Fate of buoyant and non-buoyant microplastics in the nearshore zone of uninterrupted sandy beaches, a 3D exploratory model

EMILIA ZYGARŁOWSKA

MASTER THESIS

INSTITUTE FOR MARINE AND ATMOSPHERIC RESEARCH UTRECHT

Utrecht University

Supervisors: prof. dr. H. E. de Swart & dr. A. Nnafie

Second supervisor: prof. dr. L. R. M. Maas

Student number: 0275735

July 2023

Fate of buoyant and non-buoyant microplastics in the nearshore zone of uninterrupted sandy beaches, a 3D exploratory model

Emilia M. Zygarłowska[a], Abdel Nnafie[a], Huib E. de Swart[a]

[a]Institute for Marine and Atmospheric Research (IMAU), Department of Physics, Utrecht University, Princetonplein 5, Utrecht, 3584 CC, The Netherlands

Abstract

In this study, the motion of both buoyant and non-buoyant microplastics in the nearshore zone of a single-barred beach system is investigated. Understanding the pathways and fate of microplastics in this region is crucial, as the nearshore zone is considered to be a hotspot that accumulates microplastics. The motion of microplastic particles is determined by incoming waves, currents, dispersive processes related to turbulence, and the settling velocity of the particles. To investigate the fate of floating and sinking microplastics– specifically, whether they beach, get trapped in the nearshore zone, or escape towards the open ocean– a 3D wave-averaged Lagrangian Particle Tracking Model (LPTM) is developed and employed. It was found that majority of floating microplastics released offshore eventually beach. The remaining particles stay trapped in rip circulation cells. In contrast, sinking particles released offshore tend to escape towards the open ocean. Those that manage to enter the surf zone, reside therein with only a small fraction of particles beaching. When sinking particles are released close to the shoreline, a small percentage of them is able to escape towards the surf zone and further into the open ocean. In the shoaling zone, the linear component of the Stokes drift velocity moves floating particles towards the surf zone, where they get trapped in the rip circulation. Close to the shoreline, components of the Stokes drift velocity cause microplastics to beach. Sinking particles are addtionally subject to the undertow that moves them offshore, which results in less beaching. The relative importance of processes that drive particle motion depends on the environmental conditions, such as the wave height, wave period, wave angle of incidence, but also the bathymetry and buoyancy of microplastics themselves. Results of this study are ultimately useful to improve parametrizations of beaching in models that simulate microplastics on the scale of shelf seas and oceans.

Keywords: microplastics, nearshore zone, rip current circulation, sandy beach

July 6, 2023

1. Introduction

1.1. Overview and Motivation

Plastic pollution of seas and oceans is a worldwide issue that has a growing negative impact on the environment. In particular, microplastic particles with diameters smaller than 5 mm, are likely the most abundant and harmful group of plastics present in the world oceans (Law and Thompson, 2014). Microplastics have been reported to be widely pervasive in marine habitats, including beaches and wetlands (Hidalgo-Ruz et al., 2012), and the deep sea (Van Cauwenberghe et al., 2013; Woodall et al., 2014). They are found both at the surface of the water and within the water column (Cózar et al., 2014). The main sources of microplastics in the marine environment are rivers, fragmentation of larger plastic items, and loss of cargo and fishing gear (Law and Thompson, 2014).

Understanding the pathways and fate of microplastics is crucial to maximise the efficiency of plastic waste management and attaining clean oceans (McElwee et al., 2012). For that purpose, numerical models have been developed and employed (e.g. Declerck et al., 2019; Critchell and Lambrechts, 2016; Reniers et al., 2009). Numerical Experiments are often carried out using the Lagrangian particle-tracking framework, which uses the velocity output of Eulerian hydrodynamic models to advect microplastics (Bigdeli et al., 2022). When such models are to be used to determine accumulation zones of microplastics along beaches, a spatial resolution of 50 m or less is needed, because the hydrodynamic processes in the coastal zone act on such scales (Critchell and Lambrechts, 2016). However, most of the studies investigating plastic motion focus on much larger scales and use grid sizes of several kilometres (e.g. Lebreton et al., 2012). Consequently, in such coarse-resolution models, beaching processes are parametrised (e.g. Kaandorp et al., 2020). These parametrisations are highly simplified and do not account for environmental conditions such as the wave height or wave incidence angle, or coast-specific processes that may influence the motion of microplastics. This issue partially arises from a significant knowledge gap concerning the physical processes determining the fate and transport of microplastics in coastal areas (Zhang, 2017). These processes have been identified and described (e.g. van Sebille et al., 2020; Moulton et al., 2023), however quantitative information about the relative importance of these processes is scarce. Some insights on the motion of buoyant, floating microplastics have been obtained from the analysis of surface drifters that were released in the coastal zone (e.g. Reniers et al., 2009;

2

Schönhofer and Dudkowska, 2021). However, these studies do not provide information about the fate of non-buoyant microplastics, which undergo vertical movement, owing to the complex vertical structure of waves and currents in the nearshore zone. This paper will focus on the fate of buoyant and non-buoyant microplastics in the nearshore zone of coastal seas, and in particular, the sandy beach systems.

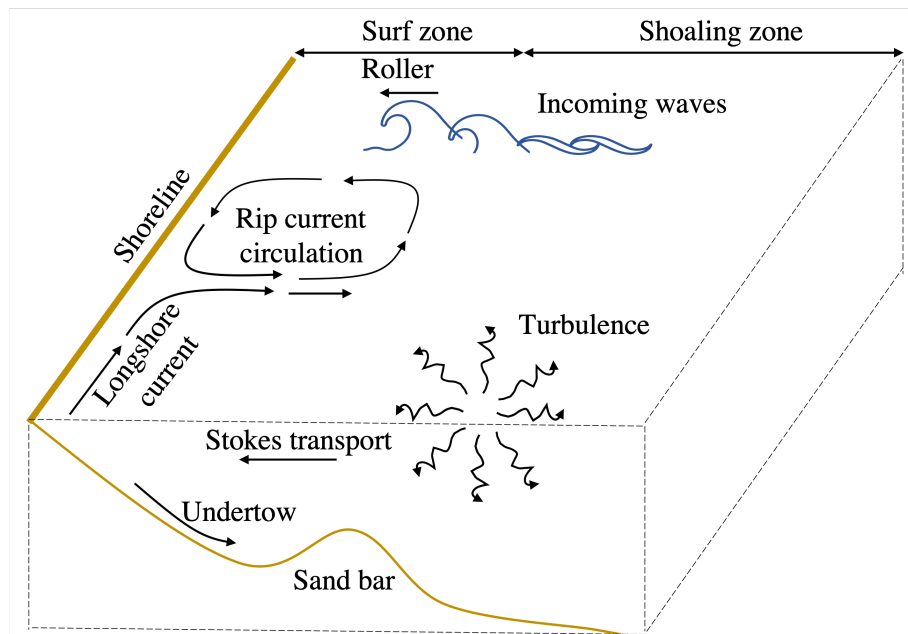## 1.2. The nearshore zone of sandy beaches

Figure 1: Physical processes occurring in the nearshore zone of a coastal sea, specifically in a single-bar beach system.

The nearshore zone (Fig. 1) covers the area of the sea and sea bottom adjacent to the shoreline and is bounded by the inner shelf on the seaward side. This zone extends between the low tide line and a boundary defined as the water depth where the largest storm waves are not able to significantly affect the bottom nor transport sediments. Typically, this occurs at depths > 0.5 times larger than the wavelength. The nearshore zone is usually $0.5 - 2.5\,\text{km}$ wide (Davidson-Arnott and Greenwood, 2003) and $10 - 20\,\text{m}$ deep at the offshore boundary (Swift, 1984). The nearshore zone consists of two subzones, namely the shoaling zone where gradual wave transformation occurs; and highly dynamic surf zone where waves break (Davidson-Arnott and Greenwood, 2003).

Sandy beaches comprise around 20% of the world's nearshore zones (Masselink and Kroon, 2009). The most common morphological feature of such environments are submerged sandbars (Davis Jr and Fitzgerald, 2009) with widths of around 100 m, and heights (i.e. crest-to-trough distance) of up to 4 m. The bars can be both alongshore uniform or have a three-dimensional nature (Davis, 1985).

The dynamical behaviour in the sandy beach systems is influenced by drivers that act on a wide range of temporal and spatial scales and which interact with each other. The three-dimensional water motion in the coastal zone is mainly driven by waves, tides and wind (Lentz and Fewings, 2012). Here, the focus is on hydrodynamic drivers related to the waves approaching the coast with periods in the order of $\mathcal{O}(10\,\mathrm{s})$, and heights of $\mathcal{O}(1\,\mathrm{m})$.
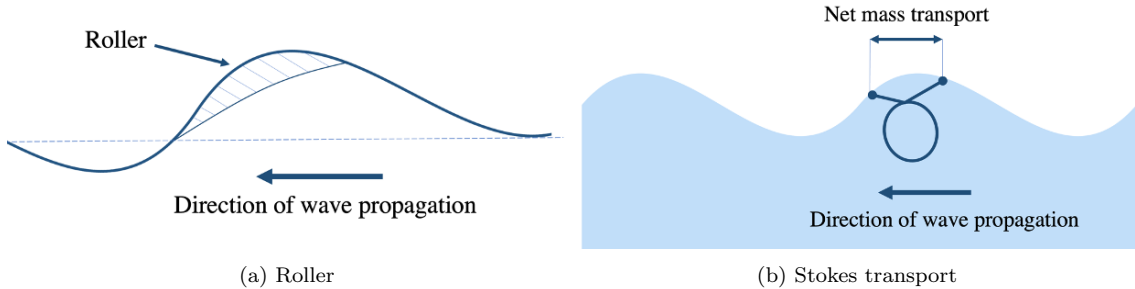

(a) Roller
(b) Stokes transport

Figure 2: (a) Path of a fluid particle in a propagating wave. The net displacement during one wave period is known as the Stokes drift velocity. (b) Roller forming on the crest of a breaking wave. Additional displacement of microplastics in the roller is in the direction of wave propagation.

Waves generated offshore enter the nearshore zone, where they experience shallower water. As a result, their wavelength decreases (shoaling), their direction of propagation changes, such that the wave crests eventually move parallel to the depth contours (refraction), and their steepness (height-to-depth ratio) increases, until they break and consequently, lose most of their energy (Holthuijsen, 2007).

As waves transition to a fully broken state, a rotating mass of water on the crest of a breaking wave in a form of a so-called roller appears (Fig. 2a; Van Dorn, 1978). Moreover, wave-breaking generates turbulence that causes mixing of the water column (Burchard et al., 2008). The increase in wave steepness causes a time-averaged imbalance between the onshore and offshore transport of water, which leads to a net onshore mass transport, known as the Stokes transport (Fig. 2b). This onshore mass transport by breaking waves is compensated by the offshore-directed return flow called the undertow, which occurs at depth below the water surface. It is driven by local differences between radiation stress and the set-up pressure gradient (Svendsen, 1984). Furthermore, breaking of the waves in the nearshore zone

4

induces velocity fields that interact with complex bottom topography. This coupling mechanism gives rise to the formation of longshore and rip currents, with velocities reaching $0.5 - 1\,\mathrm{m/s}$ (The Open University, 1999; Davidson-Arnott, 2011). Longshore currents develop when waves approach the coast at an angle with respect to shore-normal, and are directed alongshore. These currents are generated when wave momentum decreases due to breaking. This change in the momentum transfer leads to the emergence of a force with an alongshore component, balanced by the bottom friction (Longuet-Higgins and Stewart, 1964). When waves encounter an undulating three-dimensional bar, local sea level variations arise due to irregular wave breaking. Intense wave breaking occurs above the crest of the bar, while over the channels, breaking is weaker. Consequently, this results in a relatively large water level setup behind the crest and a lower setup behind the trough. The difference in setup gives rise to alongshore feeder currents, which then converge into a narrow offshore-directed rip current flowing in the rip channels. Finally, the rip current dissipates at the seaward side of the bar. The feeder currents can be altered by the longshore current arising from the obliquely incoming waves, resulting in asymmetric rip circulation cells (Davidson-Arnott, 2011).

1.3. Microplastics in the nearshore zone of sandy beaches

Microplastics in the nearshore zone of sandy beaches move due to various physical drivers (Fig. 1), many of them being different from those that act in the open ocean (Moulton et al., 2023). The primary hydrodynamic process relevant for microplastic motion is the linear component of the Stokes drift velocity, which arises from spatial variations in the velocity field experienced by microplastic particles (Stokes, 1847; Longuet-Higgins, 1969). The result is a net displacement of microplastic particles in the direction of wave propagation, which in the nearshore zone is onshore. Additional displacements of microplastics are due to the roller-induced currents, which at the surface enhance the onshore movement related to the linear component of the Stokes drift velocity, while at depths, they are in the opposite direction (Svendsen, 2005). This is compensated by the offshore-directed undertow that may move sinking particles below the surface of the water towards the open ocean. Motion of microplastics is further altered by the currents that form the rip circulation cells, where microplastics can get trapped, or they can be transported along the shoreline by the longshore currents. Furthermore, wave breaking causes increased turbulence, leading to particle dispersion and resuspension from the bottom (Deigaard, 1993). Moreover, depending on particle density and consequently its sinking velocity, transport of microplastics within the water column may serve as a major pathway for non-buoyant microplastics (Zhang, 2017), in which case the vertical structure of the

currents induced by the aforementioned processes will be of importance.

1.4. Objectives of the study

The general aim of this study is to improve the understanding of the behaviour of microplastics in the nearshore zone of uninterrupted sandy beach systems. The specific objectives are: (1) to determine the fate of microplastics entering the nearshore zone from the open ocean or through coastal sources, i.e. how many of the released microplastics beach, what are the associated beaching time scales and alongshore distribution of beached particles. Moreover, how many particles escape towards the open ocean, or get trapped in rip current circulation, (2) to quantify the relative importance of hydrodynamic processes driving the motion of floating and sinking microplastics, and (3) to investigate the sensitivity of the particle motion to environmental conditions, such as the incoming wave height, wave period, and wave angle of incidence.

To study the behaviour of microplastics at the surface of the water, but also within the water column, an idealised process-based 3D wave-averaged Lagrangian Particle Tracking Model (LPTM) is developed. This model allows for decomposition of individual hydrodynamic processes to quantify their relative importance for particle motion. Moreover, the sensitivity to input environmental conditions (wave height, wave period or wave incidence angle) can be investigated.

The description of the model and of the experimental setup is provided in Section 2. The results are presented in Section 3, followed by their discussion in Section 4. The conclusions are given in Section 5.

6

2. Materials and Methods
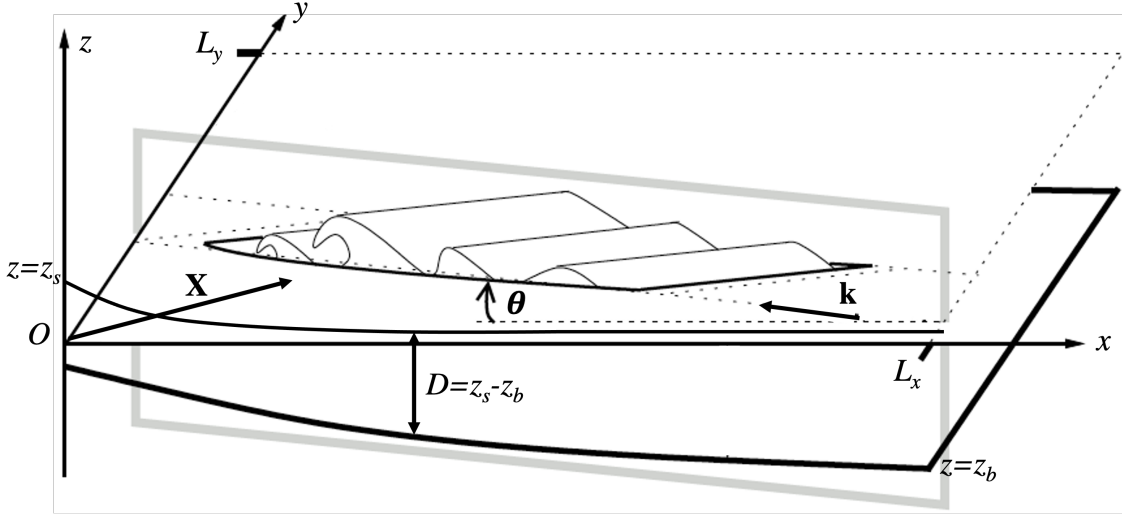
2.1. Lagrangian Particle Tracking Model

Figure 3: Model domain used for computations (adapted from Garnier et al. (2006)). The rectangular domain has sizes L_x and L_y in the cross-shore (x-axis) and longshore (y-axis) directions, respectively. The z-axis is directed vertically upwards with its origin $z = 0$ being the still water level. Depth D is the difference between the mean sea surface z_s and bed level z_b. Waves propagate in the direction of the wave vector $\mathbf{k}$ with the incidence angle θ with respect to the negative x-axis. A 3D position of a particle is represented by vector $\mathbf{X}$.

The 3D Lagrangian Particle Tracking Model (LPTM) computes particle trajectories at the surface of the water and within the water column. The focus of this study is on the motion of microplastics, but in principle LPTM can be applied to a wide range of particles, such as nutrients, plankton, etc. LPTM requires the Eulerian flow fields and wave information as input to derive the corresponding Lagrangian flow fields resulting from different hydrodynamic features that drive the motion of microplastics (described in Section 1.3).

The nearshore zone hydrodynamics, morphodynamics and particle motion are considered in a rectangular domain (Fig. 3) within the Cartesian coordinate system (O, x, y, z) with the origin O situated at a boundary separating the swash zone and the surf zone. This arbitrary line is herein referred to as the shoreline. The x-axis represents the seaward direction. The y-axis is along-shore directed. The domain is restricted by $x = 0$ at the shoreline, $x = L_x$ at the offshore boundary, and by

7

boundaries $y = 0$, and $y = L_y$ on the sides. The z-axis is directed vertically upwards with its origin $z = 0$ being the still water level.

Particle paths are determined by incoming waves, net currents, and dispersive processes related to turbulence, mostly induced by wave breaking. These paths are written as $\mathbf{X}(\mathbf{X}_0, t)$, where $\mathbf{X} = (X, Y, Z)$ is a 3D position vector, $\mathbf{X}_0$ the initial position at $t = 0$, and t is time.

In this study, the position vector $\mathbf{X}(\mathbf{X}_0, t)$ is considered on a time scale much longer than the peak period of incoming waves. Therefore, the displacements $d\mathbf{X}$ are due to the wave-averaged Lagrangian velocity $\overline{\mathbf{U}}_L(\mathbf{X}_0, t)$ that particles experience during their motion, as well as due to their settling, and Brownian motion (turbulence).
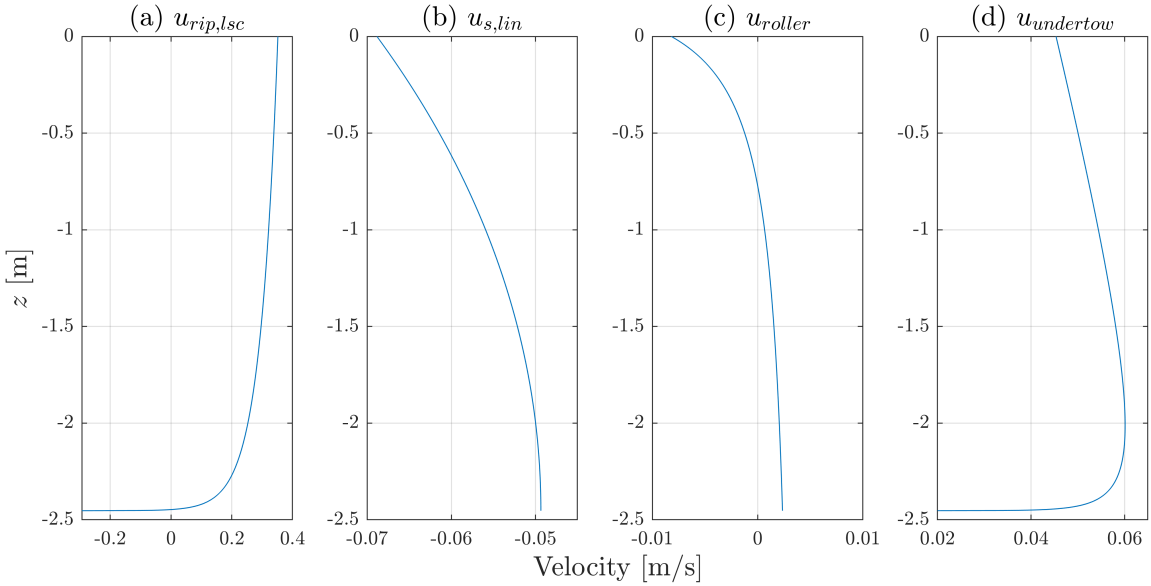

Figure 4: Example vertical profiles of the cross-shore velocity components. The profiles are computed for (a) rip and longshore currents $\mathbf{u}_{rip,lsc}$, (b) linear components of the Stokes drift velocity $\mathbf{u}_{s,lin}$, roller-induced currents $\mathbf{u}_{roller}$, and (d) the undertow $\mathbf{u}_{rip,lsc}$. Negative values represent onshore-directed currents.

Within this study, the net displacements of particles are governed by the equation comprising of the deterministic advection part and diffusive stochastic part:

$$dX = (\mathbf{U}_s + \mathbf{U}_c - w_s \mathbf{e}_z) \, dt + \boldsymbol{\sigma} \cdot d\mathbf{W} \ . \tag{1}$$

In this expression, $\mathbf{U}_s$ is the Stokes drift velocity, $\mathbf{U}_c$ the mean current, w_s is the settling velocity of a particle and $\mathbf{e}_z$ a unit vector in the vertical direction. The last

8

term on the right-hand side represents displacements resulting from the turbulence-induced Brownian motion. Here, the 3×3 tensor σ is such that $\frac{1}{2}\boldsymbol{\sigma} \cdot \tilde{\boldsymbol{\sigma}}$ (the tilde denotes a transpose) is the dispersion tensor. Furthermore, $\mathbf{W}(t)$ are the Wiener processes (also known as time-integrated white noise processes), with zero mean and unit variance. The exact expressions of the terms in Eq. 1 are given in the following sections. More information on the origin of the expression for $d\mathbf{X}$ can be found in Gardiner (1985) and Heemink (1990). In the latter sections, the sum of the components of $\mathbf{U}_s$ and $\mathbf{U}_c$ is referred to as the total Lagrangian velocity $\mathbf{U}_{tot}$, to which a corresponding total Eulerian velocity is assigned, such that $\mathbf{u}_{tot}(\mathbf{x} = \mathbf{X}) = \mathbf{U}(\mathbf{X})$.

In the nearshore zone, the Stokes drift velocity due to wave motion consists of two parts:

$$\mathbf{U}_s = \mathbf{U}_{s,lin} + \mathbf{U}_{roller} \ . \tag{2}$$

The first part is related to linear waves, while the second part emerges from non-linearities. The net displacement of a fluid particle during one wave period follows from linear wave theory (e.g. Svendsen, 2005), and by applying the Stokes formula (Stokes, 1847; Longuet-Higgins, 1969), the result in the deep water limit is

$$\mathbf{U}_{s,lin} = \frac{\omega k H_{rms}^2}{8} \frac{\cosh\left(2k(Z - z_b)\right)}{\sinh^2(kD)} \hat{\mathbf{k}} \ . \tag{3}$$

In this expression, H_{rms} is the root-mean-square wave height, D is the total mean depth, and $\omega = \sqrt{gk \tanh(kD)}$ is the wave frequency. Furthermore, $\hat{\mathbf{k}}$ is the unit vector of the wave vector $\mathbf{k}$, and k- its magnitude. Thus, $\mathbf{U}_{s,lin}$ is in the direction of wave propagation and in the coastal zone, this is usually onshore.

All variables on the right-hand side of Eq. 3 are obtained from the output of a morphodynamical model- Morfo55 (Garnier et al., 2006, 2008). This model solves depth-averaged shallow-water equations with sediment transport and bed updating. For given incident waves at the offshore boundary of the model domain, it calculates the wave variables ω, $\mathbf{k}$, H_{rms}, and wave angle θ. Moreover, it computes the depth-averaged currents, mean sea surface z_s and bed level z_b, from which the total mean depth $D = z_s - z_b$ is obtained. More information about Morfo55 is given in the Appendix A.

The contribution that adds to the Stokes drift velocity and is due to the wave roller (roller-induced current) reads

$$\mathbf{U}_{roller} = \frac{1}{4}\left(cf(Z) - \frac{1}{2}\gamma_m c\right)\exp\left(-\frac{\gamma_m^2 D^2}{H_{rms}^2}\right)\hat{\mathbf{k}} \ . \tag{4}$$

Here, c is the phase speed, $\gamma_m = \frac{H_b}{D}$ is the wave breaker index, with H_b being the critical wave height for which the waves break. It is assumed that $\gamma_m = 0.62$. Expression 4 originates from the fact that, when microplastics are in the roller of a breaking wave, the amplitude of wave-induced velocity is different than that of linear waves $\frac{1}{2}\gamma_m c$. This results in modified displacements of particles, which adds to the linear Stokes drift velocity in the upper part of the water column, but which opposes the Stokes drift closer to the bed (Svendsen, 2005). It is assumed that at a fixed point rollers are present during a quarter of a wave period, which explains the factor $\frac{1}{4}$. Following Van Dorn (1978), the vertical distribution of wave-induced velocity in the roller reads

$$f(Z) = \left(c_1 + \frac{c_2 \xi}{c_3 - \xi} \right) , \tag{5}$$

where $c_1 = 0.154$, $c_2 = 0.106$, $c_3 = 1.125$, and $\xi = \frac{Z - z_b}{D}$. The last term in Eq. 4 represents the probability that a roller occurs, i.e.,

$$P(H \geq H_b) = \int_{H_b}^{\infty} p(H) dH , \tag{6}$$

The explicit expression for this probability, as appears in Eq. 4 is obtained by assuming $p(H) = \exp\left(-\frac{H_b^2}{H_{rms}^2} \right)$ to be the Rayleigh distribution for wave heights H.

The mean current driving the particle motion results from two contributions:

$$\mathbf{U}_c = \mathbf{U}_{rip,lsc} + \mathbf{U}_{undertow} . \tag{7}$$

The first contribution represents the wave-driven currents. The vertical structure of $\mathbf{U}_{rip,lsc}$ is assumed to be logarithmic, i.e.

$$\mathbf{U}_{rip,lsc} = <\mathbf{U}_{rip,lsc}> f_2(Z) , \tag{8}$$

where

$$f_2(Z) = \frac{\ln\left(\frac{Z - z_b}{z_0} \right)}{\ln\left(\frac{D}{z_0} \right) - 1} , \tag{9}$$

in which the depth-averaged $< f_2(Z) >= 1$. The depth-averaged currents $< \mathbf{U}_{rip,lsc} >$ are computed as

$$<\mathbf{U}_{rip,lsc}> = \mathbf{U}_{m55} - \frac{M}{\rho D} \sin \theta \mathbf{e}_y . \tag{10}$$

In this expression, $\mathbf{U}_{m55}$ is the velocity calculated by Morfo55, $\mathbf{e}_y$ is the unit vector in the longshore direction, $M = \frac{E}{c}$ is the wave-induced mass transport velocity, where

the energy density of waves $E = \frac{1}{8}\rho g H_{rms}^2$, with acceleration due to gravity $g = 9.81\,\mathrm{ms}^{-2}$, and water density $\rho = 1024\,\mathrm{kgm}^{-3}$. The reason that the mass transport velocity due to waves is subtracted from $\mathbf{U_{m55}}$ is that the current itself is needed. Note that there is no correction for wave-induced mass transport, as that is taken care of by the undertow, which is discussed hereafter.

The second contribution in Eq. 7, $\mathbf{U}_{undertow}$, describes the return flow perpendicular to the shoreline, compensating for the depth-mean onshore transport due to waves. Following Rattanapitikon and Shibayama (2000), the vertical distribution of the undertow is formulated as

$$\mathbf{U}_{undertow} = \left(\frac{\epsilon}{\rho}\right)^{\frac{1}{3}}\left[\left(\frac{1}{2} - \frac{Z - z_b}{h_t}\right) + \alpha\left(\ln\left(\frac{Z - z_b}{h_t}\right) + 1\right)\right]\mathbf{e}_x + <\mathbf{U}_m> . \quad (11)$$

Here, the wave-induced, depth-averaged Stokes return flow in the cross-shore direction $<\mathbf{U}_m> = \frac{M}{\rho D}\cos\theta\mathbf{e}_x$, with unit vector in the cross-shore direction $\mathbf{e}_x$. The above expression contains ϵ (computed with Morfo55), which is the dissipation of wave energy due to breaking and bottom friction, $h_t = D - \frac{H_{rms}}{2}$ is the level of the wave troughs, and the calibration coefficient $\alpha = 0.21$.

An example of vertical profiles of the currents described above is given in Fig. 4.

The unresolved processes, such as the explicit effect of turbulence due to wave breaking, are accounted for by introducing stochastic terms in the Lagrangian model. It is assumed that

$$\frac{1}{2}\boldsymbol{\sigma}\cdot\tilde{\boldsymbol{\sigma}} = \begin{pmatrix} A_H & 0 & 0 \\ 0 & A_H & 0 \\ 0 & 0 & A_v \end{pmatrix}, \quad (12)$$

in which

$$A_H = \nu_0 + f_h H_{rms}\left(\frac{\epsilon}{\rho}\right)^{\frac{1}{3}}, \quad (13)$$

and

$$A_v = \nu_0 + f_v D\left(\frac{\epsilon}{\rho}\right)^{\frac{1}{3}} \quad (14)$$

are the horizontal (Battjes, 1975) and vertical (Reniers et al., 2004) dispersion coefficients, respectively. In these expressions, $\nu_0 = 0.001\,\mathrm{m}^2/\mathrm{s}$ is a numerical parameter and $f_h = 1$ and $f_v = 0.01$ are the calibration factors for the horizontal and vertical components of the stochastic process, respectively. The expression $\left(\frac{\epsilon}{\rho}\right)^{\frac{1}{3}}$ defines a measure of turbulence. Therefore

11

$$\boldsymbol{\sigma} = \begin{pmatrix} (2A_H)^{\frac{1}{2}} & 0 & 0 \\ 0 & (2A_H)^{\frac{1}{2}} & 0 \\ 0 & 0 & (2A_v)^{\frac{1}{2}} \end{pmatrix} \tag{15}$$

determines the effectiveness of turbulence on particle motion.

2.2. Handling of microplastics at the boundaries

Once the microplastics reach the shoreline ($X < 4\,\mathrm{m}$), they are identified as "beached", thus inactive and are removed from further computations. When microplastics cross the lateral boundaries of the rectangular domain ($Y < 0$ or $Y > L_y$), they are temporarily marked as "escaped". However, a periodic boundary is applied, and thus, the microplastics are reintroduced in the model domain on the opposite lateral boundary. Microplastics that cross the offshore boundary ($X > L_x$) escape to the open sea and are removed from further computations. To prevent microplastics from leaving the model domain through the surface and the bottom, a closed boundary condition is applied, i.e. microplastics that cross the surface or the bottom are set to remain at these boundaries ($Z > z_s \implies Z = z_s$ and $Z < -z_b \implies Z = -z_b$). Microplastics that are deposited on the bottom, can be resuspended if the upward-directed vertical turbulence is strong enough to exceed the settling velocity of the microplastics.

2.3. Numerical methods

Each velocity component described in Section 2.1 is evaluated in an Eulerian frame of reference on a rectangular grid, which is composed of grid cells, that are defined by Δx and Δy (cross-shore and longshore grid cell lengths, respectively). To obtain the Lagrangian velocity of a particle at each time step, an interpolation of the Eulerian velocities to the time-varying particle position $\mathbf{X}$ is needed. The necessary velocity interpolations are performed using a linear scheme. The deterministic advection part of LPTM is then solved numerically using the Runge-Kutta integrator of the first order (e.g. Fujimura et al., 2014; Beron-Vera et al., 2008).

The increment of a stochastic contribution is added at each time-step such that dW_i becomes $\Delta \mathbf{W}_i = \boldsymbol{\sigma}_{ij} G_i \sqrt{\Delta t}$. Here, G_i is a value taken from the Gaussian distribution of random numbers with mean $= 0$ and standard deviation $= 1$, and Δt is the time-step of the Lagrangian model. The $\sqrt{\Delta t}$ is used to ensure that the variance $< \Delta \mathbf{W}_i \Delta \mathbf{W}_j > = \boldsymbol{\sigma}_{ij} \Delta t$ increases with Δt as assumed for the random walk processes (Mannela, 2002).

2.4. Setup of the Experiments

As a prototype sandy beach system, the single-barred beach of Duck (North Carolina, the US) is used to investigate the motion of microplastics. For this, the numerical morphodynamic model Morfo55 is run from an initial condition that only has a single alongshore uniform bar (Fig. 5) based on the equation of Yu and Slinn (2003)

$$z_b(x) = -a_0 - a_1 \left(1 - \frac{\beta_2}{\beta_1} \right) \tanh \left(\frac{\beta_1 x}{a_1} \right) - \beta_2 x + a_2 \exp \left[-5 \left(\frac{x - x_c}{x_c} \right)^2 \right], \quad (16)$$

where $x_c = 80\,\mathrm{m}$ is the bar location, $a_2 = 1.5\,\mathrm{m}$ is the bar amplitude, $a_0 = 0.25\,\mathrm{m}$ is the water depth at the swash/surf zone boundary, and $a_1 = 2.97\,\mathrm{m}$. $\beta_1 = 0.075$ and $\beta_2 = 0.0064$ are the beach slopes on the shore and offshore sides of the bar, respectively.
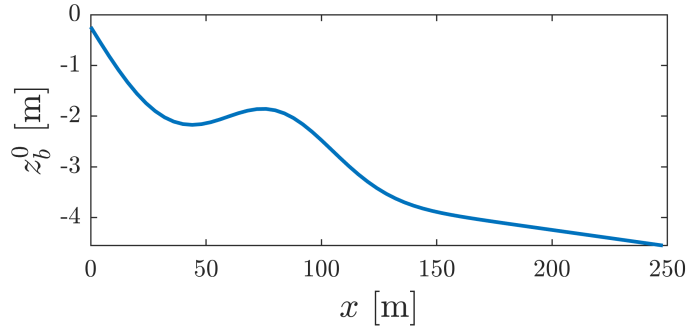

Figure 5: Initial alongshore uniform bottom profile at Duck, North Carolina

The rectangular model domain extends to $L_x = 250\,\mathrm{m}$ in the cross-shore direction and $L_y = 400\,\mathrm{m}$ in the longshore direction, with a spatial resolution (Δx and Δy) of $2\,\mathrm{m}$ in both directions. Morfo55 model is run on a rectangular domain until a fully saturated three-dimensional bottom topography is obtained. Details on how that is done are in Garnier et al. (2008). The result bottom level, depth, wave characteristics, and velocity fields, are used to construct the Lagrangian velocity fields.

Next, the particle tracking model is run on the same domain. The time step Δt used for the computations of the microplastics trajectories equals $3\,\mathrm{s}$, and the duration of each simulation is $3\,\mathrm{hours}$. To initiate the simulations, 100 microplastic

13

particles are released at the surface of the water ($Z_0 = z_s$), at the offshore boundary ($X_0 = 240$ m) of the model domain evenly spaced in the longshore direction, with spacing between each particle set to 4 m. Additionally, Experiments with microplastics released 14 m away from the shoreline are performed. To obtain robust and reliable results, accounting for the inherent randomness of the stochastic component of the model, 10 realisations of particle motion are performed from each initial position.

This is, first, above all, to study the statistics related to the motion of microplastics: how many of them beach, get trapped, or escape towards the open ocean; how long does it take for them to beach, and what is the distribution of beached microplastics over the shoreline. In the default case (Table 1), the input wave height is set to 1 m, the wave angle of incidence to $0°$, and the wave period to 7.5 s. Two sets of experiments are conducted to investigate the behaviour of both floating (Experiments $default\_1a$, $default\_1b$) and sinking microplastics (Experiments $default\_2a$, $default\_2b$), with sinking velocity w_s set to 0 m/s and $5 \cdot 10^{-4}$ m/s, respectively. When considering floating microplastics it is assumed that they cannot sink from the surface and thus, they only experience surface currents. For these simulations, the output of Morfo55 remains unchanged and only the settling velocity and/or release location of the microplastics differs. For each configuration, the relative contributions of the hydrodynamic processes are assessed of all components that contribute to the total Lagrangian velocity as is experienced by the particles.

To investigate the effect of environmental conditions on particle motion, a series of experiments for various input wave conditions is performed, as specified in Table 1. These also concern new simulations with Morfo55. In particular, the effect of varying incoming wave height (Experiments $H1.2\_1$, $H1.2\_2a$, $H1.2\_2b$), wave period (Experiments $T6\_1$, $T6\_2a$, $T6\_2b$), and wave incidence angle (Experiments $A5\_1$, $A5\_2a$, $A5\_2b$) is studied. For Experiments involving obliquely incoming waves, the model domain is extended to 800 m.

2.5. Analysis of model results

Various indicators are computed to describe the motion of microplastics. Trajectories of microplastics, provide insights into the overall motion patterns of the analysed particles. The raw output of LPTM containing information on the location of every particle at each time step is further analysed to address the specific objectives of the study. Firstly, the fate of microplastics is analysed based on their position at the end of each simulation. As described in Section 2.2, there are three possible fates of particles: "beached", "escaped", and "trapped". These outcomes are expressed as a percentage of the total number of the released particles. Further-

Table 1: Input wave conditions and parameter values used for different experiments.

H_{rms}[m]	T[s]	θ[°]	w_s[m/s]	Release location	Experiment name
				offshore	default_1a
			0	shoreline	default_1b
1	7.5	0		offshore	default_2a
			$5 \cdot 10^{-4}$	shoreline	default_2b
			0	offshore	H1.2_1
1.2	7.5	0		offshore	H1.2_2a
			$5 \cdot 10^{-4}$	shoreline	H1.2_2b
			0	offshore	T6_1
1	6	0		offshore	T6_2a
			$5 \cdot 10^{-4}$	shoreline	T6_2b
			0	offshore	A5_1
1	7.5	5		offshore	A5_2a
			$5 \cdot 10^{-4}$	shoreline	A5_2b

more, the time scales involved in the motion of microplastics are investigated. In particular, percentages of released microplastics arriving at the shoreline as a function of time are computed. Moreover, mean t_{mean} and standard deviation t_{std} of the time it takes for particles to beach are calculated. To identify the accumulation zones of microplastics on the beach, the probability distribution of the alongshore position of the beached particles is computed.

The total velocity experienced by the particle reads $\mathbf{U}_{tot}$, and consists of four components $\mathbf{U}_\alpha$, where $\alpha = s, lin/roller/rip, lsc/undertow$. The latter relate to the linear component of the Stokes drift velocity, additional drift due to wave rollers, rip and longshore currents, and the undertow (only for experiments involving sinking particles). To each of these total Lagrangian velocities, a corresponding total Eulerian velocity $\mathbf{u}_\alpha(\mathbf{x})$ is assigned, such that $\mathbf{u}_\alpha(\mathbf{x} = \mathbf{X}) = \mathbf{U}_\alpha(\mathbf{X})$. The velocity scale associated with turbulence is expressed as $\mathbf{u}_{turb} = \left(\frac{\epsilon}{\rho}\right)^{\frac{1}{3}}$. To quantify the relative importance of hydrodynamic processes, velocity fields of $\mathbf{u}_{s,lin}$, $\mathbf{u}_{roller}$, $\mathbf{u}_{rip,lsc}$, $\mathbf{u}_{undertow}$, $\mathbf{u}_{turb}$ together with their root-mean-square rms value are generated

$$rms = \sqrt{\frac{\sum_{i=1}^{n} u_i^2}{n}} \ . \tag{17}$$

Here, n is the number of grid cells and u_i is the velocity value in a grid cell. The relative importance of hydrodynamic processes is expressed as a fraction $rms_\alpha/rms_{u_{tot}}$

, where $rms_{u_{tot}}$ is the root-mean-square velocity of the total Eulerian current $\mathbf{u}_{tot}$, and rms_α is the root-mean-square velocity of $\mathbf{u}_{s,lin}/\mathbf{u}_{roller}/\mathbf{u}_{rip,lsc}/\mathbf{u}_{undertow}/\mathbf{u}_{turb}$. These fractions are also computed for different regions within the nearshore zone. In particular, for the shoaling zone $rms_{shoaling}$ ($x > 130\,\mathrm{m}$), the bar region rms_{bar} ($30\,\mathrm{m} < x < 100\,\mathrm{m}$), and the shoreline region $rms_{shoreline}$ ($x < 20\,\mathrm{m}$).

3. Results

As described in Section 2.1, motion of microplastics is determined by incoming waves, net currents, and dispersive processes related to turbulence. These characteristics are based on wave and current fields, but also the bathymetry. These fields are derived from Morfo55, which is run until a fully saturated state is reached. The resulting bathymetry represents an undulating bar pattern comprising of alternating crests and rip channels. For information about the spatial distribution of wave height H_{rms}, wave vector $\mathbf{k}$, wave angle of incidence θ, and dissipation of wave energy ϵ needed for further computations in $default\_1$, $H1.2\_1$, $T6\_1$, and $A5\_1$ Experiments, see Appendix B.

3.1. Fate of microplastics

Snapshots of the motion of floating microplastics that are released at the offshore boundary of the model domain (Experiment $default\_1a$) are shown in Fig. 6a-d. Microplastics firstly move onshore in the shoaling zone ($x > 130\,\mathrm{m}$) and ultimately enter the surf zone (Fig. 6a). Here, they move over the undulating bar, where they are initially advected onshore over the crests (Fig. 6b). Subsequently, they get trapped in rip circulation cells (Fig. 6c-d). Eventually, 23% of released microplastics reside in the surf zone by locally circulating, while the remaining 77% beach. The beached microplastics tend to accumulate behind the rip channels (Fig. 6e). On average, microplastics reach the shoreline within $42\,\mathrm{min}$ ($t_{std} = 22\,\mathrm{min}$) after release (Fig. 6f).

In Experiment $default\_1b$, all floating microplastics released close to the shoreline beach shortly after the beginning of the simulation, so no further analysis is needed.

Fig. 7a shows the projection of trajectories of sinking microplastics onto the horizontal plane (Experiment $default\_2a$). In this case, 42% of sinking microplastics enter the surf zone, while 58% escape towards the open ocean. Those that reach the surf zone, behave similarly to the floating particles in Experiment $default\_1a$: they move over the crests and then they are transported near the bottom in the rip channels. Eventually, only 6% of sinking microplastics beach, while 36% circulate in the rip current cells. Notably, the accumulation of beached microplastics behind the rip channels is more pronounced than in Experiment $default\_1a$ as seen in Fig. 7c.
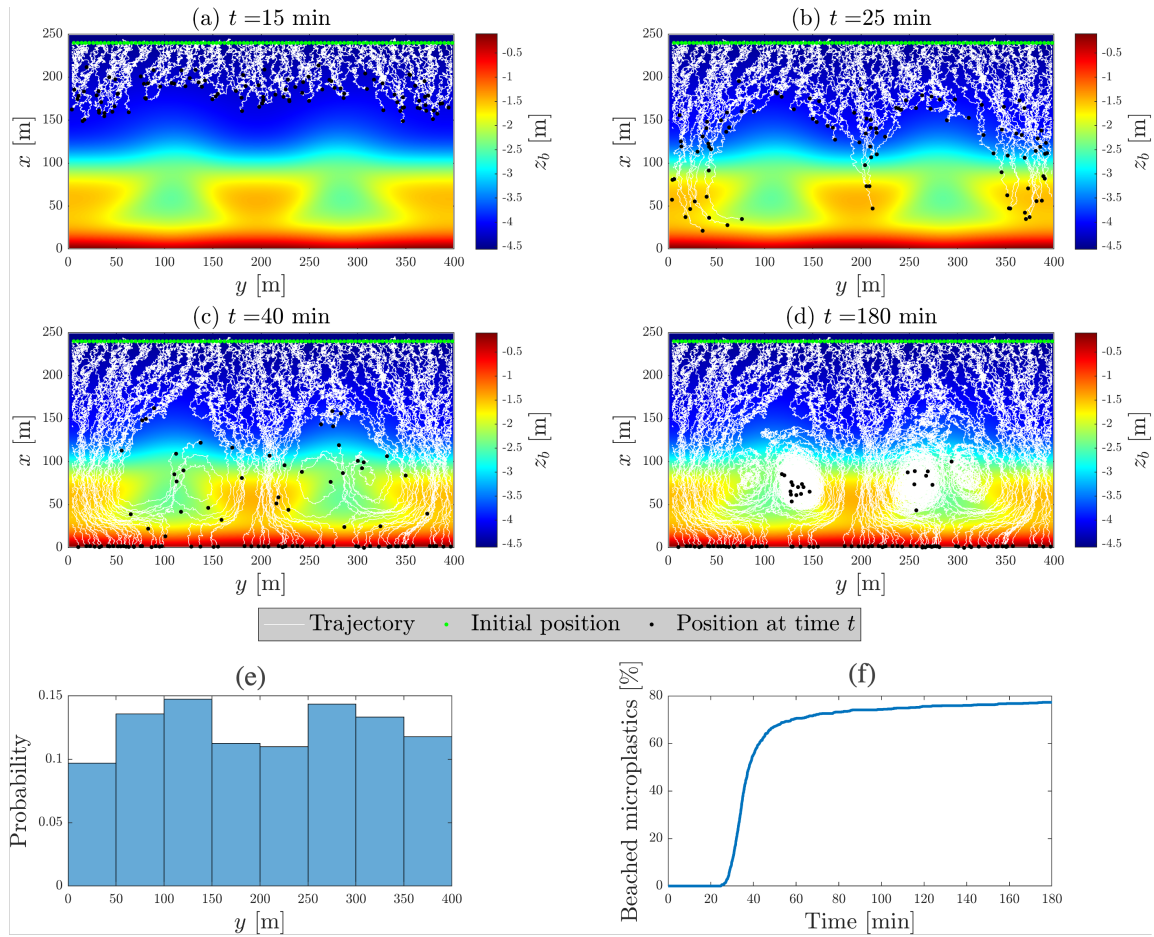
16

Figure 6: (a)-(d) Snapshots of the example trajectories (white lines) of floating microplastics for Experiment $default\_1a$ at times (a) $t = 15\,\mathrm{min}$, (b) $t = 25\,\mathrm{min}$, (c) $t = 40\,\mathrm{min}$, (d) $t = 180\,\mathrm{min}$. Colours represent the bed level z_b. Note that, for plotting purposes, motion of 100 out of 1000 particles released at the offshore boundary is shown. Green and black markers indicate the initial position and particle position at time t, respectively. (e) Probability distribution of the alongshore position of the beached microplastics. (f) Percentage of released microplastics arriving at the shoreline as a function of time.

From Fig. 7e it appears, that microplastics reach the shoreline considerably slower than in the $default\_1a$ Experiment. In this case, the average arrival time is $122\,\mathrm{min}$ ($t_{std} = 34\,\mathrm{min}$).

When sinking microplastics are released close to the shoreline (Experiment $default\_2b$), Fig. 7b,c,e reveals that most of them (87%) beach within a mean time of $7\,\mathrm{min}$ ($t_{std} = 17\,\mathrm{min}$). These particles tend to beach behind the rip channels. Interestingly,
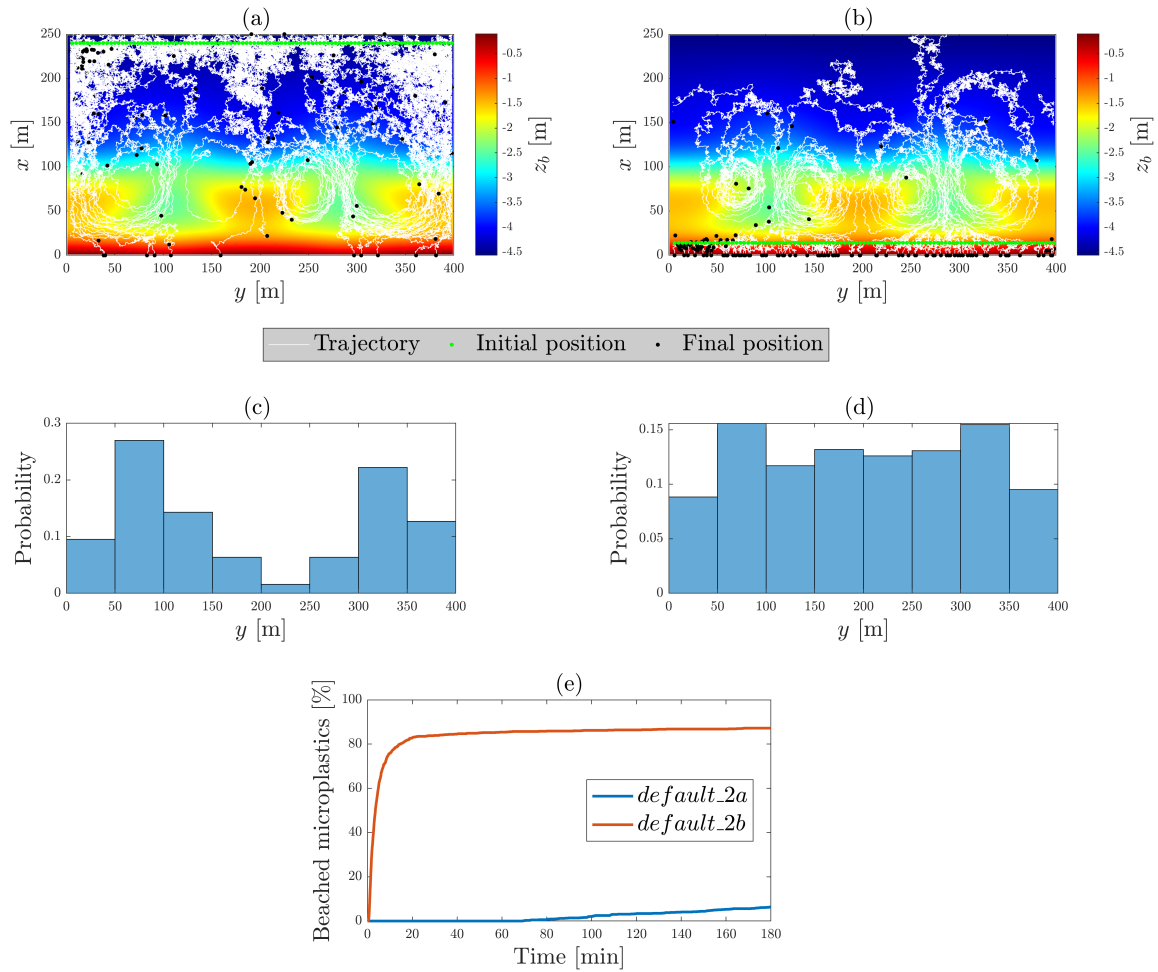
Figure 7: (a)-(b) Snapshots of the example trajectories (white lines) of sinking (settling velocity=$5 \cdot 10^{-4}$ m/s) microplastics for Experiments (a) $default\_2a$ and (b) $default\_2b$. The top view of the motion of 100 out of 1000 particles released at the offshore boundary plotted over the bed level z_b (colours) is shown. Green and black markers indicate the initial position and final particle position, respectively. (c)-(d) As in Fig 6e, but for Experiments (c) $default\_2a$ and (d) $default\_2b$. (e) As in Fig 6f, but for for Experiments $default\_2a$ (blue line), and $default\_2b$ (orange line).

13% of microplastics are able to escape from the shoreline. These microplastics get trapped in rip circulation cells (10%), or escape to open sea (3%).

3.2. Relative importance of hydrodynamic processes for microplastics motion

The spatial variation of currents is shown in Fig. 8a. In the shoaling zone, before wave breaking ($x > 130$ m), the total Eulerian current $\mathbf{u}_{tot}$ is onshore-directed and
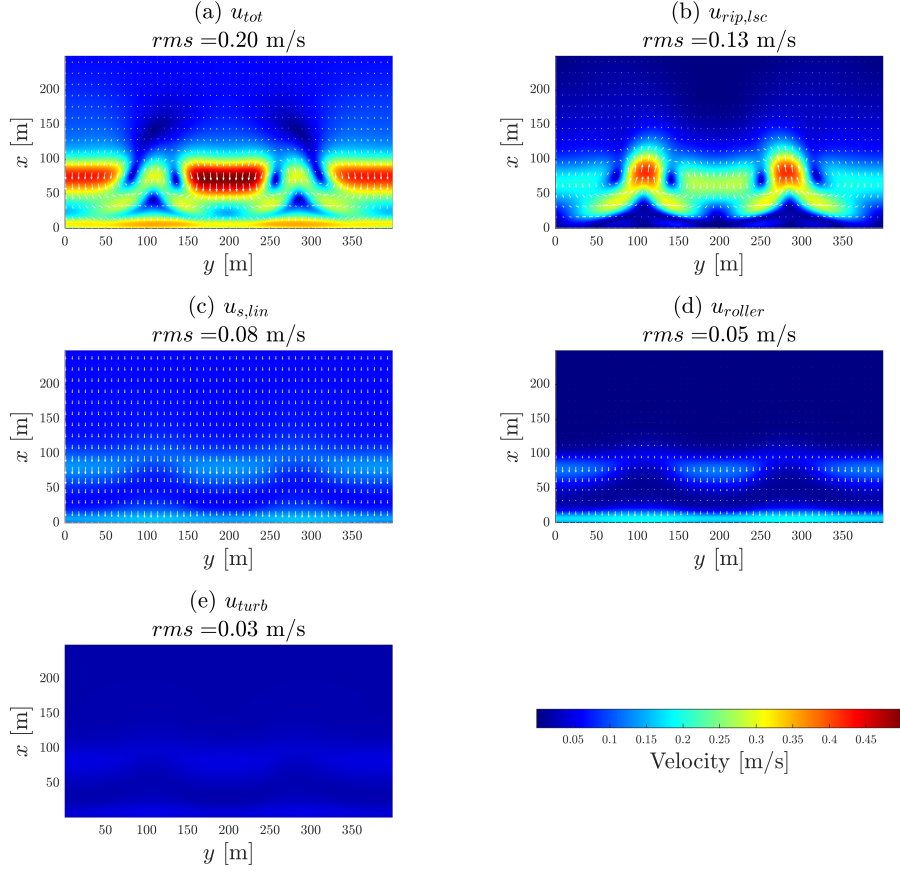
Figure 8: Spatial distribution of the Eulerian current velocities (colours) and their direction (arrows); rms refers to a root-mean-square, with the mean taken over the domain. If a particle is at a certain position $\mathbf{X}$, it will experience velocity $\mathbf{u}_{tot}(x = \mathbf{X})$ and additionally, it will be subject to stochastic displacements due to turbulence. (a) total velocity field $\mathbf{u}_{tot}$ (b) $\mathbf{u}_{rip,lsc}$, (c) $\mathbf{u}_{s,lin}$, (d) $\mathbf{u}_{roller}$. (e) Velocity scale of the horizontal turbulence $\mathbf{u}_{turb} = \left(\frac{\epsilon}{\rho}\right)^{\frac{1}{3}}$.

attains velocities of $0.12\,\text{m/s}$. Over the undulating bar, a circulation pattern emerges with strong offshore-directed currents in the rip channels reaching $0.30\,\text{m/s}$, while over the crests, onshore-directed currents reach $0.50\,\text{m/s}$. Shoreward of the bar, $\mathbf{u}_{tot}$ has a longshore component with maximum velocity of $0.30\,\text{m/s}$. Close to the shoreline, $\mathbf{u}_{tot}$ attains velocities of $0.36\,\text{m/s}$ and remains onshore directed.

The total Eulerian currents result from different components, whose spatial pattern is depicted in Fig. 8b-e. Moreover, their relative importance in different regions
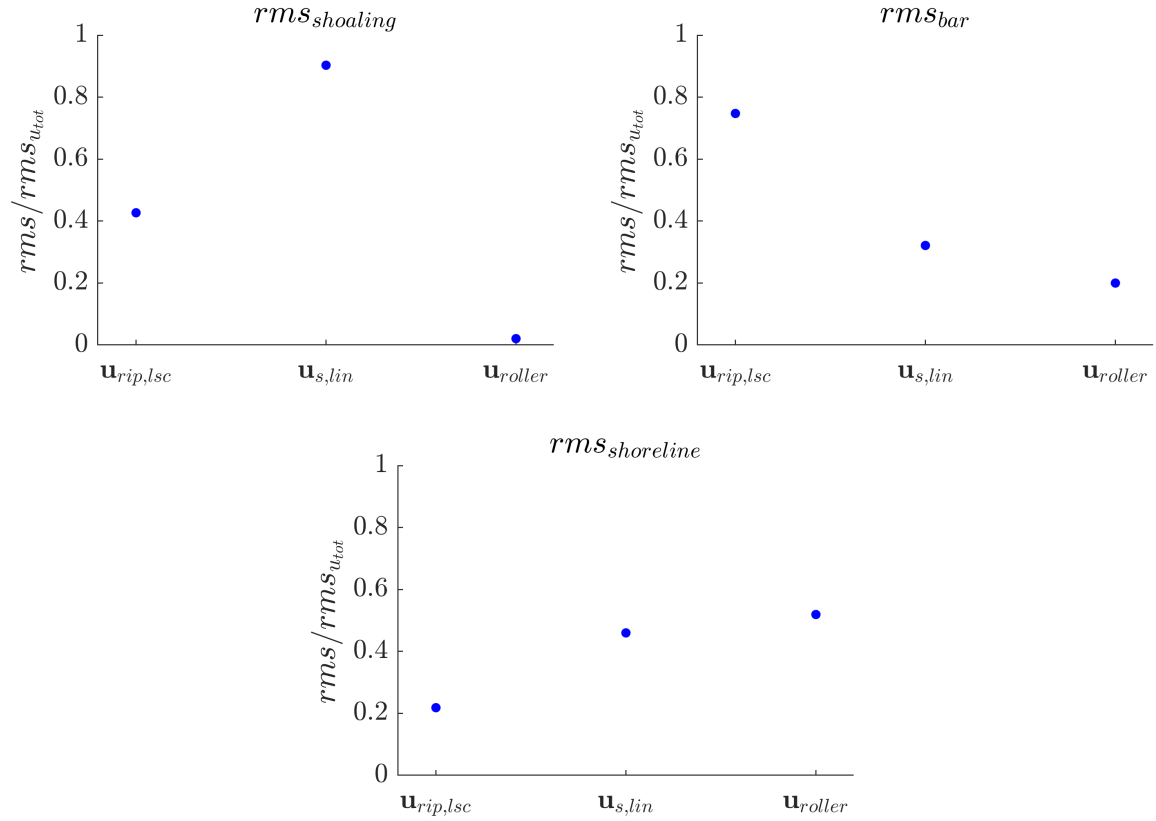
Figure 9: Relative importance of hydrodynamic processes expressed as a fraction $rms/rms_{u_{tot}}$, where $rms_{u_{tot}}$ is the root-mean-square velocity of the total Eulerian current $\mathbf{u}_{tot}$, and rms is the root-mean-square velocity of $\mathbf{u}_{rip,lsc}$, $\mathbf{u}_{s,lin}$, $\mathbf{u}_{roller}$. The relative importance is shown for three regions: (a) shoaling zone ($x > 130\,\mathrm{m}$, (b) bar region ($30\,\mathrm{m} < x < 100\,\mathrm{m}$), and (c) shoreline region ($x < 20\,\mathrm{m}$).

of the considered domain is quantified in Fig. 9. It turns out that the linear component of the Stokes drift velocity $\mathbf{u}_{s,lin}$ has the largest rms-value, where rms stands for the root-mean-square value when taking the average over the domain. In the sand bar region, the circulation pattern arises primarily from the wave-induced currents $\mathbf{u}_{rip,lsc}$ forming a rip circulation. Additionally, over the crests of the bar, the linear component of the Stokes drift velocity $\mathbf{u}_{s,lin}$ increases in magnitude, and wave breaking induces rollers leading to additional onshore currents $\mathbf{u}_{roller}$. In the rip channels, the combined effect of $\mathbf{u}_{s,lin}$ and $\mathbf{u}_{roller}$ attenuates the offshore-directed rip currents, while amplifying the onshore-directed $\mathbf{u}_{rip,lsc}$ over the crests. The longshore component of the currents observed shoreward of the bar is attributed to the feeder currents associated with the rip circulation. Close to the shoreline, both components of the
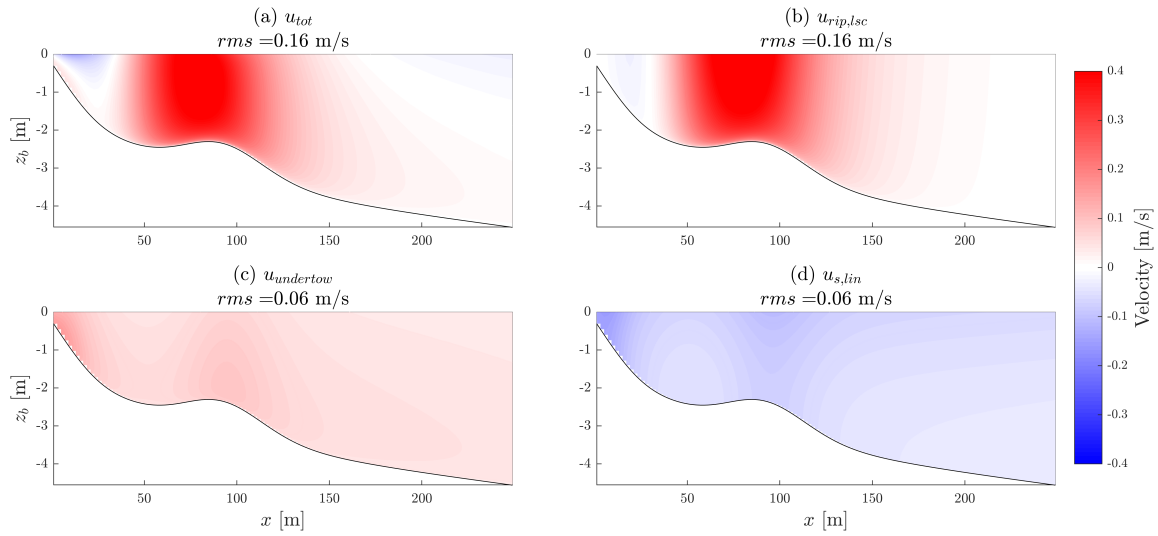
Figure 10: Vertical structure of the cross-shore components of the net Eulerian currents computed for the cross-sections through the rip channel ($y = 290\,\mathrm{m}$). Panels represent the cross-shore velocity components of (a) the total Eulerian current $\mathbf{u}_{tot}$, (b) rip and longshore currents $\mathbf{u}_{rip,lsc}$, (c) the undertow $\mathbf{u}_{undertow}$, (d) the linear component of the Stokes drift velocity $\mathbf{u}_{s,lin}$. Negative values indicate onshore-directed currents. The roller-induced current $\mathbf{u}_{roller}$ is negligible and thus, not plotted here.

Stokes drift velocity ($\mathbf{u}_{s,lin}$ and $\mathbf{u}_{roller}$) reach their maximum absolute values due to intense wave breaking, which makes these processes the dominating contributors in this region. The magnitude of the velocity induced by horizontal turbulence $\left(\frac{\epsilon}{\rho}\right)^{\frac{1}{3}}$ is most pronounced in the regions where wave breaking occurs, particularly over the bar and close to the shoreline, behind the rip channels.

Regarding the motion of floating particles, the results of Figures 8 and 9 indicate that floating microplastics enter the surf zone due to the linear component of the Stokes drift velocity. In the surf zone, their orbits are affected by the currents within the rip circulation cells. Since in the bar region, the onshore currents are stronger than the offshore currents, microplastics that do not get trapped in the cells, are ultimately washed ashore due to the components of the Stokes drift velocity. Horizontal turbulence causes dispersion of microplastics, however, these additional displacements are small compared to the total Lagrangian velocity that a particle experiences at each time step.

When focusing on sinking microplastics, additional velocity components, in particular, the settling velocity and the undertow, play a role. Fig. 10 shows the Eulerian velocity fields in a cross-section through a rip channel ($y = 290\,\mathrm{m}$). In the shoaling

21

zone ($x > 130$ m), the total Eulerian current $\mathbf{u}_{tot}$ is onshore-directed close to the surface of the water with velocities reaching 0.12 m/s. At depths of around 2 m below the surface, $\mathbf{u}_{tot}$ becomes offshore-directed with velocities of 0.10 m/s. The highest velocities are reached in the bar region. Here, the strong offshore-directed currents attain velocities of 0.45 m/s. Shoreward of the bar, the current is onshore-directed at the surface, and offshore close to the bottom.

Both in the shoaling zone, as well as in the region shoreward of the bar, onshore-directed currents at the surface arise from the linear component of the Stokes drift velocity. The offshore currents at depths are due to the undertow. Over the bar, the currents in the rip circulation cells contribute the strongest to the total current throughout the water column. In the channels between the sand bars, the offshore-directed rip current has the same direction as the undertow, while over the crests, they almost cancel each other, such that the total current is mainly due to the linear component of the Stokes drift velocity. The roller-induced currents emerge in the regions of wave breaking and are negligible compared to other contributions. Both horizontal and vertical turbulence are the most intense in the bar region and close to the shoreline

The implications of these results are that, when sinking microplastics are released offshore, they are initially transported close to the surface by the linear component of the Stokes drift velocity. However, at depth, the horizontal turbulence becomes relatively strong. Together with the undertow, this causes particles to escape offshore. Once microplastics enter the surf zone at depth below the surface, their motion is influenced by the currents in the rip circulation cells and by the undertow, which leads to their trapping in the surf zone. Strong undertow and weak components of the Stokes drift velocity close to the bottom, prevent microplastics from reaching the shoreline. When sinking microplastics are released close to the shoreline, most of them beach due to the combined effect of the Stokes drift velocity components. Some particles are able to escape, in particular those, which are released in the vicinity of a rip channel, because in that region both undertow and the rip current are directed seaward. Notably, vertical turbulence is strong compared to the settling velocity of microplastics, which causes their easy resuspension from the bottom. Therefore, the particles move within the water column as suspended load and do not reside at the bottom.

3.3. Sensitivity of particle motion to environmental conditions

Motion of floating microplastics for Experiments $H1.2\_1$, $T6\_1$, and $A5\_1$ is shown in Fig. 11. When the height of incoming waves has been increased from 1 m to 1.2 m with respect to the default setting, 25% of floating microplastics get trapped in the
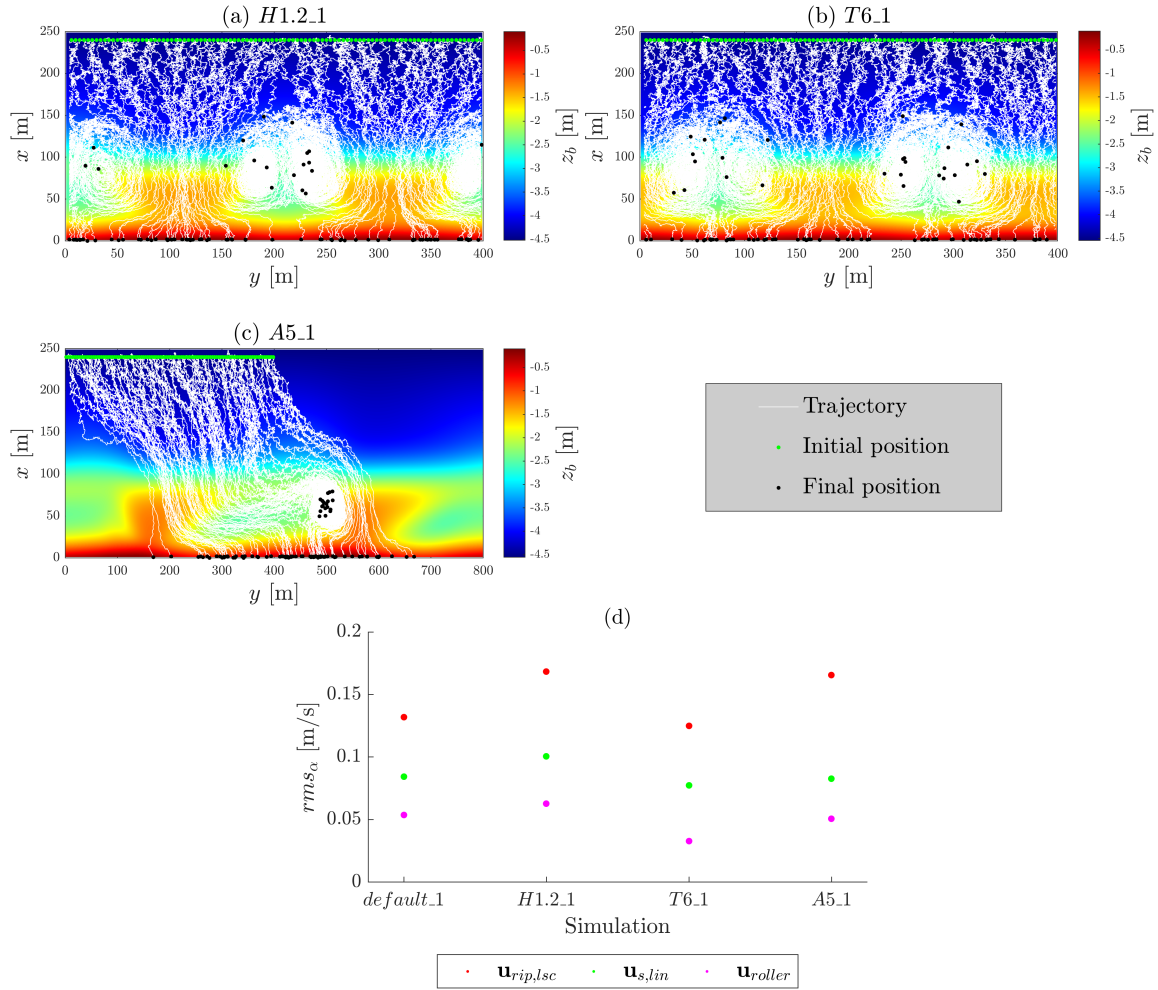
22

Figure 11: (a)-(c) Snapshots of the example trajectories (white lines) of floating microplastics for Experiments (a) $H1.2\_1$, (b) $T6\_1$, (c) $A5\_1$. Note that, for plotting purposes, motion of 100 out of 1000 particles released offshore plotted over the bed level z_b (colours) is shown. Green and black markers indicate the initial and final position of microplastics, respectively. (d) Root-mean-square velocity of different components of the total Eulerian current $_{tot}$. The root-mean-square velocity rms_α is computed for $\mathbf{u}_{rip,lsc}$ (red), $\mathbf{u}_{s,lin}$ (green), $\mathbf{u}_{roller}$ (magenta). The mean refers to an average over the whole domain.

nearshore zone, while 75% beach, which is slightly less than in the default case. The mean time of 29 min that the particles need to arrive at the shoreline is considerably shorter (t_{std} of 18 min). Interestingly, increased wave height results in more beaching of sinking microplastics released offshore (Experiment $H1.2\_2a$). In that case, 11% of microplastics arrive at the shoreline within 106 min on average ($t_{std} = 38$ min).

23

Similarly to the $default\_2b$ Experiment, most (88%) of the sinking microplastics released close to the shoreline (Experiment $H1.2\_2b$) beach.

Compared to the default setting, the period of incoming waves has been reduced from 7.5 s to 6 s in Experiments $T6\_1$, $T6\_2a$, and $T6\_2b$. It appears that shorter wave period results in less beaching (64%) of floating microplastics. Similarly to the default case, these microplastics reach the shoreline within 41 min on average ($t_{std} = 21$ min). The amount of beaching (6%), as well as the involved time scales for Experiment $T6\_2a$ are similar to those of $default\_2a$. However, there are more microplastics (61%) escaping towards the open ocean. As a consequence, fewer particles enter the surf zone where they would get trapped in the rip circulation. More microplastics (13%) released close to the shoreline (Experiment $T6\_2b$) are able to escape and get trapped in the nearshore zone.

When waves approach the shoreline at an angle, an alongshore current emerges resulting in an oblique bar orientation. As a result, in Experiment $A5\_1$, 77% of floating particles beach, which is the same as in the $default\_1a$ Experiment. However, it takes longer for particles to arrive at the shoreline, with a mean arrival time of 49 min ($t_{std} = 20$ min). In the $A5\_2a$ Experiment, 56% of released microplastics enter the surf zone, none of which beach. These particles stay within the surf zone and are transported alongshore instead. Only 6% of sinking microplastics released close to the shoreline (Experiment $A5\_2b$) manage to escape towards the surf zone where they are transported along the shoreline.

When input environmental conditions are changed, the spatial pattern of different components of the total Eulerian current, as well as the bottom topography are altered. The root-mean-square velocities for different Experiments are shown in Fig. 11d. It appears that the increased wave height results in stronger currents compared to the default case. Moreover, rip channels become narrower while crests wider. Consequently, the spatial extent of the rip circulation cells is smaller. The rms velocities of currents in the $T6\_1$ Experiment are notably smaller than in $default\_1$. In this case, rip circulation cells become wider. In the $A5\_1$ Experiment, the strength of both the linear component of the Stokes drift velocity, as well as the roller-induced currents are approximately the same as in the default case. However, the value of $rms_{urip,lsc}$ becomes notably higher, which is related to the formation of an alongshore current. Moreover, spacing between rip channels increases.

A graphical summary of the sensitivity analysis can be found in Appendix C. These results indicate that higher wave height affects the motion of microplastics resulting in a higher proportion of floating microplastics being trapped in the now stronger rip circulation. The opposite is observed for sinking microplastics. In this case, particles are not easily trapped in smaller rip circulation cells, which leads to

more beaching. Moreover, beaching occurs within a shorter time frame. The fate of microplastics appears to be sensitive to the shorter wave period. Here, wider rip circulation cells capture more particles resulting in less beaching, however beaching time scales seem not to be influenced. It appears that the longshore current emerging when waves approach the shoreline at an angle acts as a barrier that sinking microplastics are not able to cross.

4. Discussion

The main findings of this study are that, regardless of the environmental conditions, majority of floating microplastics released offshore eventually beach. The remaining particles stay trapped in rip circulation cells and do not escape towards the open ocean. This finding is consistent with the results reported in MacMahan et al. (2010). In contrast, sinking particles released offshore tend to escape towards the open ocean. Those that manage to enter the surf zone, reside therein with only a small fraction of particles beaching. When sinking particles are released close to the shoreline, a small percentage of them is able to escape towards the surf zone and further into the open ocean. This specifically applies to particles that are initially at the landward end of a rip channel.

Our results confirm those of Reniers et al. (2009) and Fujimura et al. (2014), that the linear component of the Stokes drift velocity is crucial for both floating and sinking microplastics to enter the surf zone. Non-buoyant microplastics that are released offshore are additionally subject to the undertow that prevents microplastics from entering the surf zone and reaching the shoreline. Sinking microplastics residing near the bottom are typically transported over the shoals first and then get trapped in rip circulation cells. At the surface, the linear component of the Stokes drift velocity dominates the particle motion and facilitates beaching. Consequently, a small fraction of floating microplastics gets trapped in the rip circulation. Additionally, the roller-induced Stokes drift velocity, which was not considered in Fujimura et al. (2014), amplifies onshore currents leading to more beaching of floating microplastics. Since horizontal turbulence is weak compared to the net currents, microplastics on average are transported in the direction of the net currents. Strong vertical turbulence relative to the settling velocity of studied microplastics causes them to move as suspended load.

The motion of microplastics is influenced by wave conditions because they affect the strength of the relevant currents, wave breaking, as well as the 3D bottom topography and the spatial pattern of currents. As such environmental conditions are important in explaining the variability in the behaviour of microplastics. Wave period appeared to greatly affect the amount of beaching, while wave height impacted

25

the timescales involved. Microplastics were found to be transported alongshore when waves approached the nearshore zone at an angle with respect to the shore-normal, thereby resulting in microplastics being transported alongshore. Even a very small θ considered in this study notably influenced the motion of microplastics.

We wish to emphasize that the model used in this study is designed to gain understanding of the fundamental processes and interactions that are involved in a poorly understood motion of microplastics in the nearshore zone. In terms of what Murray (2003) phrases, our model is an exploratory model that can provide insights into the role of various mechanisms that drive the motion of microplastics. Indeed, in contrast to more complex numerical models, such as the one used by Reniers et al. (2009), our model enables decomposition and analysis of individual processes driving microplastics motion greatly improving the understanding of the involved transport mechanisms.

Our model considers a limited number of drivers of microplastics in the nearshore zone and the conclusions apply for the specific settings considered. It would be interesting in future work to include additional drivers. In particular, windage and wind-driven currents might be of importance for particles protruding out of the water (van Sebille et al., 2020). Moreover, results by Kaandorp et al. (2022) reveal that tides play an important role in beaching of microplastics. The presence of streaming in the wave boundary layer, which was not taken into account in this study, results in onshore mass transport (Longuet-Higgins and Stoneley, 1953) and thus, can affect the motion of sinking microplastics. Furthermore, the model results are representative for rip-channelled, uninterrupted sandy beaches only. Although this is a common beach type, the surf zone circulation is affected by the bathymetry and it is worth investigating other beach types, e.g. multi-barred or tidal inlet systems.

Furthermore, some assumptions regarding the behaviour of the microplastics themselves can be revisited. It is expected that biofouling and fragmentation of plastics, as is considered in e.g. Zhang (2017); Kaandorp et al. (2021) are not important to include, given the relatively short times (hours to days) that particles spend in the nearshore zone. Moreover, it is possible that microplastics are buried in sediment after reaching the bottom (Moreira et al., 2016; Costa et al., 2011), while in this study the applied boundary condition allows for their resuspension due to strong vertical turbulence.

A limited number of possible environmental conditions was considered in this study. Application to a wider range of environmental conditions and inclusion of other processes will contribute to further insight results. Furthermore, a thorough analysis of the sensitivity of results to the value of the sinking velocity is considered

to be an important topic for future research. As reported in various studies (e.g. Hidalgo-Ruz et al., 2012) microplastics with small sinking velocities are easily resuspended and washed ashore, while microplastics with higher sinking velocities remain on the bottom for longer and thus tend to reside away from the shoreline. Results of this study are ultimately useful to improve parametrizations of beaching in models that simulate microplastics on the scale of shelf seas and oceans.

5. Conclusions

As pollution of beaches by microplastics has become a major issue of concern, it is important to understand the motion and fate of microplastics in the coastal zone. This study showed that majority of floating microplastics beach, while a notable fraction gets trapped in rip circulation cells. When sinking microplastics are released offshore, they tend to escape towards the open ocean and the remaining particles reside within the nearshore zone with a low quantity reaching the shoreline. Interestingly, a notable part of the sinking microplastics released close to the shoreline is able to escape towards the open ocean. Furthermore, the most important hydrodynamic processes driving microplastics motion vary depending on the region within the nearshore zone and the settling velocity of microplastics. In the shoaling zone, close to the surface of the water, the linear component of the Stokes drift velocity moves microplastics towards the surf zone. At depth, undertow causes sinking microplastics to escape into the open ocean. Rip circulation is the dominant hydrodynamic process in the bar region causing microplastics to get trapped in the surf zone. Close to the shoreline, roller-induced currents and the linear component of the Stokes drift velocity cause microplastics to beach. Additionally, sinking microplastics are subject to the undertow, which moves them away from the shoreline. It was found that wave height influences the time scales within which microplastics beach, while the wave period affects the amount of beaching. When waves approach the coast under an angle with respect to the shore-normal, an alongshore current acts as a barrier between the surf zone and the shoreline that sinking microplastics are not able to cross. This study provides valuable insights into the motion of microplastics in the nearshore zone of sandy beaches, and as such can contribute to improving future modelling studies of the nearshore zone and parametrizations used in large-scale models, as well as the coastal waste management efforts.

Appendix A. Morfo55 model

As explained in the main text, this model developed by Garnier et al. (2006) is used to generate wave fields, depth-mean currents and bottom topography in the

27

nearshore zone for given offshore wave conditions. The output of Morfo55 is used to compute the currents that advect the particles. Morfo55 is a nonlinear numerical model, which solves depth-averaged shallow-water equations, equations for height, period, wavelength and angle of surface waves, coupled to equations that describe sediment transport and bed updating. The domain considered is identical to that shown in Fig. 3.

The system consists of four independent variables, namely x, y, z, and t (instantaneous time), where $i\,(i = 1, 2)$ represents the projection of the vector on the x_i-axis.

The wave transformation is described using wave height $H\,(x, y, t)$, the wave vector $\boldsymbol{k}(x, y, t)$ with its modulus k, and the wave frequency $\omega(x, y, t)$. Here, the root-mean-square average of the wave height $H_{rms}\,(x, y, t)$ is used to describe random waves based on the Rayleigh Probability Density Function (Longuet-Higgins, 1952). Interchangeably with H_{rms}, the wave energy density $E\,(x, y, t)$ can be used. The wave vector, computed using the dispersion relation, is used to derive the wave numbers $k_1\,(x, y, t) = k\cos\theta$ and $k_2\,(x, y, t) = k\sin\theta$, and the wave angle $\theta(x, y, t) = \arctan\left(-\frac{k_2}{k_1}\right)$ defined as the angle between the wave vector and the negative x-axis.

Moreover, the instantaneous surf zone dynamics are described by sea water level $z_s\,(x, y, t)$, bed level $z_b\,(x, y, t)$, and the components of the flow velocity vector $u_i\,(x, y, t)$. The mean bed level can also be described using $h(x, y, t)$, the deviation of the bed from the time- and longshore mean topography $z_b^0(x)$, representing the long-term bottom averaged over the longshore direction, such that

$$h\,(x, y, t) = z_b\,(x, y, t) - z_b^0\,(x)\ . \tag{A.1}$$

The bed evolution is described based on the depth-averaged sediment concentration $C(x, y, t) = \alpha/D$, with $D\,(x, y, t) = z_s - z_b$ being the total mean depth and α- the stirring factor.

As the goal is to describe slow, large-scale morphological changes coupled to net currents, some simplifications are needed. In particular, the above-mentioned variables are averaged over a wave period T. This way the fastest phenomena, namely the wave orbital motion and the turbulent motions are not explicitly solved, but their effects are parametrised, thus enabling the description of the long-term morphodynamics.

Furthermore, shallow water theory is applied, based on the fact that the horizontal scales are much larger than the vertical scales. As a result, the depth-averaged horizontal velocity is defined.

The system of unknowns described above is solved using wave- and depth-averaged

equations, which represent a fully coupled system, computed as follows:

$$\frac{\partial E}{\partial t} + \frac{\partial}{\partial x_j}\left((u_j + c_{gj})\,E\right) + S'_{ij}\frac{\partial u_j}{\partial x_i} = -\epsilon\,, \tag{A.2}$$

$$k \sin\theta = k_0 \sin\theta_0\,, \tag{A.3}$$

$$\frac{\partial D}{\partial t} + \frac{\partial}{\partial x_j}\left(Du_j\right) = 0\,, \tag{A.4}$$

$$\frac{\partial u_i}{\partial t} + u_j\frac{\partial u_i}{\partial x_j} = -g\frac{\partial z_s}{\partial x_i} - \frac{1}{\rho D}\frac{\partial}{\partial x_j}\left(S'_{ij} - S''_{ij}\right) - \frac{\tau_{bi}}{\rho D}\,. \tag{A.5}$$

$$\frac{\partial z_b}{\partial t} + \frac{\partial q_j}{\partial x_j} = 0\,, \tag{A.6}$$

Repeated indices in a term mean a summation over all its values, according to the Einstein's summation convention. The equations represent Eq.A.2 the wave energy equation, Eq.A.3 the Snell's law, Eq.A.4 the water mass conservation, Eq.A.6 the sediment mass conservation. Here, c_g is the group velocity vector, $E = \frac{1}{8}\rho g H_{rms}^2$, with acceleration due to gravity $g = 9.81\,\mathrm{ms}^{-2}$, and water density $\rho = 1024\,\mathrm{kgm}^{-3}$. Furthermore, S'' is the wave radiation stress tensor (Longuet-Higgins and Stewart, 1964), S'' is the turbulent Reynolds stress tensor (Battjes, 1975). Dissipation rate ϵ results from wave breaking (Thornton and Guza, 1983) and bottom friction (Horikawa et al., 1988). In the Snell's law (Eq. A.3), k_0 and θ_0 are the wave number and the wave angle at the seaward boundary. The bed shear stress vector is denoted by τ_b (Mei, 1992). The horizontal sediment flux vector q is based on the total load formula from Soulsby (1997).

Appendix B. Wave information

Appendix C. Sensitivity analysis

References

J. A. Battjes. Modelling of turbulence in the surfzone. *Symposium on Modelling Techniques, American Society of Civil Enigneers, San Francisco*, pages 1050–1061, 1975.

F. J. Beron-Vera, M. J. Olascoaga, and G. J. Goni. Oceanic mesoscale eddies as revealed by lagrangian coherent structures. *Geophysical Research Letters*, 35(12), 2008. doi: 10.1029/2008GL033957.
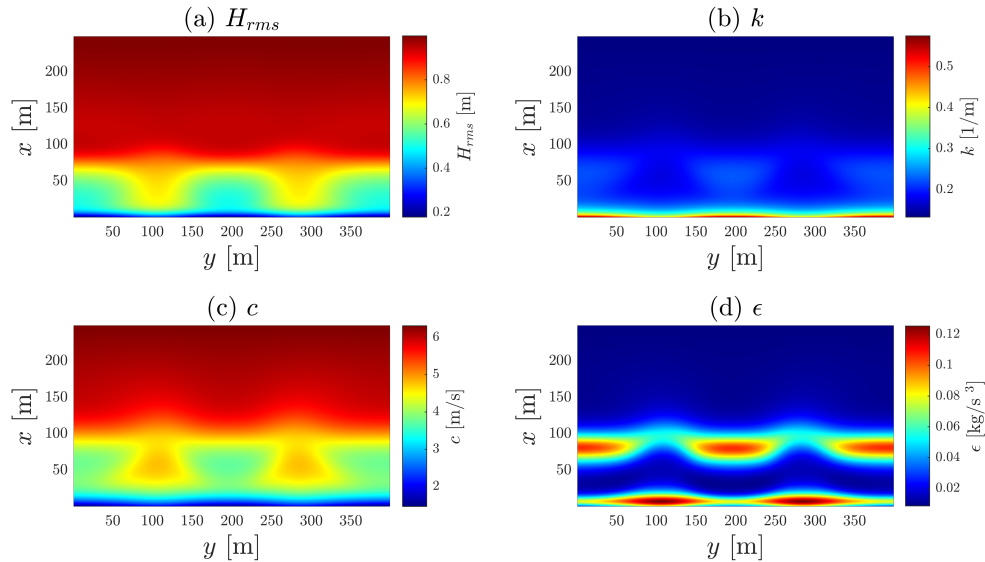
Figure B.12: Wave information obtained from Morfo55 for Experiment $default\_1$. (a) spatial distribution of the wave height H_{rms}, (b) wave number k, (c) phase speed c, and (d) energy dissipation due to wave breaking ϵ.

M. Bigdeli, A. Mohammadian, A. Pilechi, and M. Taheri. Lagrangian modeling of marine microplastics fate and transport: The state of the science. *Journal of Marine Science and Engineering*, 10(4), 2022. ISSN 2077-1312. doi: 10.3390/jmse10040481.

H. Burchard, P. D. Craig, J. R. Gemmrich, H. van Haren, P.-P. Mathieu, H. M. Meier, W. A. M. N. Smith, H. Prandke, T. P. Rippeth, E. D. Skyllingstad, W. D. Smyth, D. J. Welsh, and H. W. Wijesekera. Observational and numerical modeling methods for quantifying coastal ocean turbulence and mixing. *Progress in Oceanography*, 76(4):399–442, 2008. ISSN 0079-6611. doi: 10.1016/j.pocean.2007.09.005.

M. Costa, J. Silva-Cavalcanti, C. Barbosa, J. Portugal, and M. Barletta. Plastics buried in the inter-tidal plain of a tropical estuarine ecosystem. *Journal of Coastal Research*, 64:339–343, 2011. ISSN 07490208, 15515036.

K. Critchell and J. Lambrechts. Modelling accumulation of marine plastics in the coastal zone; what are the dominant physical processes? *Estuarine, Coastal and Shelf Science*, 171:111–122, 2016. ISSN 0272-7714. doi: https://doi.org/10.1016/j.ecss.2016.01.036.
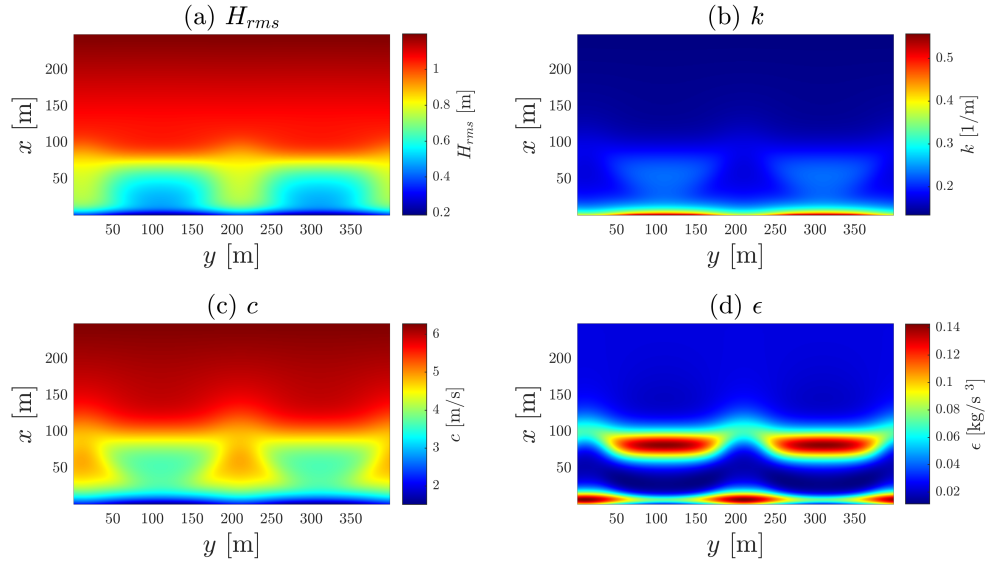
(a) H_{rms} (b) k (c) c (d) ϵ

Figure B.13: As in B.12, but for Experiment $H1.2\_1$.

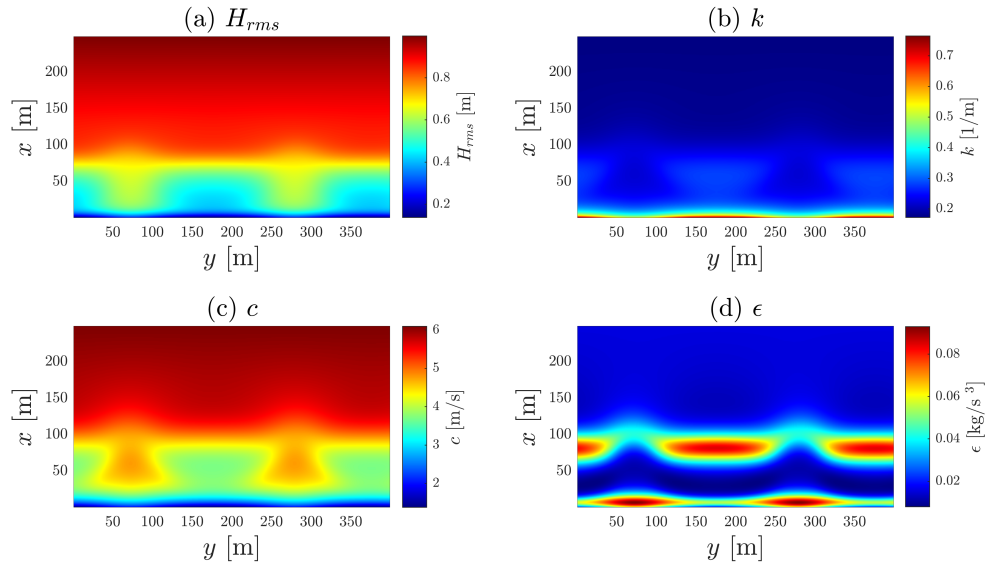(a) H_{rms} (b) k (c) c (d) ϵ

Figure B.14: As in B.12, but for Experiment $T6\_1$.

A. Cózar, F. Echevarría, J. I. González-Gordillo, X. Irigoien, B. Úbeda, S. Hernández-
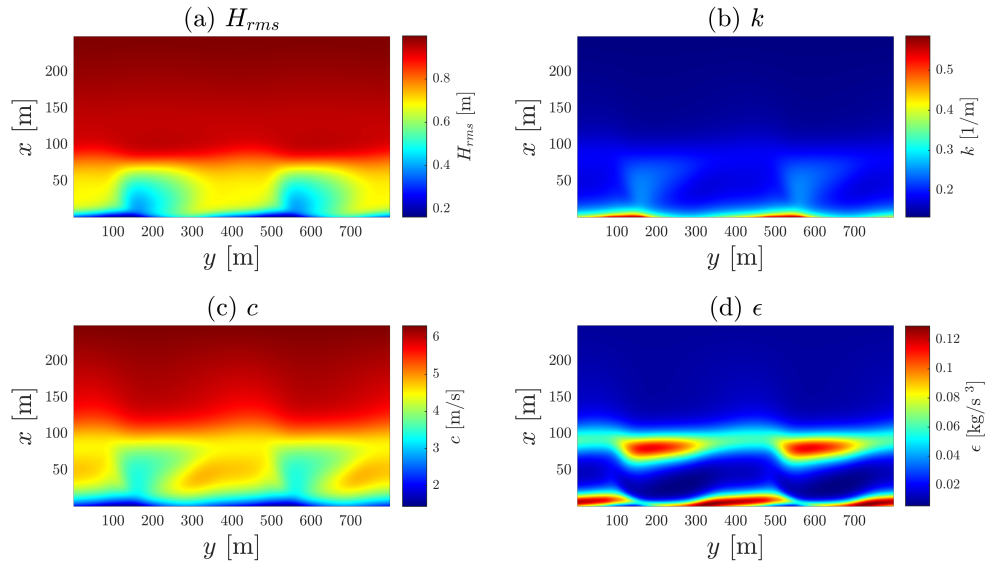
31

Figure B.15: As in B.12, but for Experiment $A5\_1$.

León, Álvaro T. Palma, S. Navarro, J. G. de Lomas, A. Ruiz, M. L. F. de Puelles, and C. M. Duarte. Plastic debris in the open ocean. *Proceedings of the National Academy of Sciences*, 111(28):10239–10244, 2014. doi: 10.1073/pnas.1314705111.

R. Davidson-Arnott. Wave-dominated coasts. *Treatise on Estuarine and Coastal Science*, 3:73–116, 12 2011. doi: 10.1016/B978-0-12-374711-2.00305-3.

R. Davidson-Arnott and B. Greenwood. *Waves and sediment transport in the nearshore zone*, pages 43–60. Encyclopedia of Life Support Systems (EOLSS) Publishers Paris, France, 2003.

R. A. Davis. *Beach and Nearshore Zone*, pages 379–444. Springer New York, New York, NY, 1985. ISBN 978-1-4612-5078-4. doi: 10.1007/978-1-4612-5078-4_6.

R. A. Davis Jr and D. M. Fitzgerald. *Beaches and Coasts*. John Wiley & Sons, 2009.

A. Declerck, M. Delpey, A. Rubio, L. Ferrer, O. C. Basurko, J. Mader, and M. Louzao. Transport of floating marine litter in the coastal area of the southeastern Bay of Biscay: A Lagrangian approach using modelling and observations. *Journal of Operational Oceanography*, 12(sup2):S111–S125, 2019. doi: 10.1080/1755876X.2019.1611708.

R. Deigaard. A note on the three-dimensional shear stress distribution in a surf zone. *Coastal Engineering*, 20(1):157–171, 1993. ISSN 0378-3839. doi: 10.1016/0378-3839(93)90059-H.

A. G. Fujimura, A. J. H. M. Reniers, C. B. Paris, A. L. Shanks, J. H. MacMahan, and S. G. Morgan. Numerical simulations of larval transport into a rip-channeled surf zone. *Limnology and Oceanography*, 59(4):1434–1447, 2014. doi: 10.4319/lo.2014.59.4.1434.

C. W. Gardiner. *Handbook of stochastic methods for physics, chemistry and the natural sciences*, volume 13. 1985.

R. Garnier, D. Calvete, A. Falques, and M. Caballeria. Generation and nonlinear evolution of shore-oblique/transverse sand bars. *Journal of Fluid Mechanics*, 567: 327–360, 2006. doi: 10.1017/S0022112006002126.

R. Garnier, D. Calvete, A. Falqués, and N. Dodd. Modelling the formation and the long-term behavior of rip channel systems from the deformation of a longshore bar. *Journal of Geophysical Research*, 113:1–18, 2008. doi: 10.1029/2007JC004632.

A. W. Heemink. Stochastic modelling of dispersion in shallow water. *Stochastic Hydrology and Hydraulics*, 4:161–174, 1990. doi: 10.1007/BF01543289.

V. Hidalgo-Ruz, L. Gutow, R. C. Thompson, and M. Thiel. Microplastics in the marine environment: A review of the methods used for identification and quantification. *Environmental Science & Technology*, 46(6):3060–3075, 2012. doi: 10.1021/es2031505.

L. Holthuijsen. *Waves in Oceanic and Coastal Waters*. Cambridge University Press, 2007. doi: 10.2277/0521860288.

K. Horikawa et al. *Nearshore dynamics and coastal processes: Theory, measurement, and predictive models*. University of Tokyo press Tokyo, 1988.

M. L. A. Kaandorp, H. A. Dijkstra, and E. van Sebille. Closing the Mediterranean marine floating plastic mass budget: Inverse modeling of sources and sinks. *Environmental Science & Technology*, 54(19):11980–11989, 2020. doi: 10.1021/acs.est.0c01984.

M. L. A. Kaandorp, H. A. Dijkstra, and E. van Sebille. Modelling size distributions of marine plastics under the influence of continuous cascading fragmentation. *Environmental Research Letters*, 16(5):054075, may 2021. doi: 10.1088/1748-9326/abe9ea.

M. L. A. Kaandorp, S. L. Ypma, M. Boonstra, H. A. Dijkstra, and E. van Sebille. Using machine learning and beach cleanup data to explain litter quantities along the dutch north sea coast. *Ocean Science*, 18(1):269–293, 2022. doi: 10.5194/os-18-269-2022.

K. L. Law and R. C. Thompson. Microplastics in the seas. *Science*, 345(6193): 144–145, 2014. doi: 10.1126/science.1254065.

L.-M. Lebreton, S. Greer, and J. Borrero. Numerical modelling of floating debris in the world's oceans. *Marine Pollution Bulletin*, 64(3):653–661, 2012. ISSN 0025-326X. doi: 10.1016/j.marpolbul.2011.10.027.

S. J. Lentz and M. R. Fewings. The wind- and wave-driven inner-shelf circulation. *Annual Review of Marine Science*, 4(1):317–343, 2012. doi: 10.1146/annurev-marine-120709-142745.

M. Longuet-Higgins. On the transport of mass by time varying ocean current. *Deep Sea Research*, 5:431–447, 1969. doi: 10.1016/0011-7471(69)90031-X.

M. Longuet-Higgins and R. Stewart. Radiation stresses in water waves; a physical discussion, with applications. *Deep Sea Research and Oceanographic Abstracts*, 11 (4):529–562, 1964. ISSN 0011-7471. doi: 10.1016/0011-7471(64)90001-4.

M. S. Longuet-Higgins. On the statistical distribution of the heights of sea waves. *Journal of Marine Research*, 11(3):245–266, 1952.

M. S. Longuet-Higgins and R. Stoneley. Mass transport in water waves. *Philosophical Transactions of the Royal Society of London. Series A, Mathematical and Physical Sciences*, 245(903):535–581, 1953. doi: 10.1098/rsta.1953.0006.

J. H. MacMahan, J. Brown, J. Brown, E. Thornton, A. J. H. M. Reniers, T. Stanton, M. Henriquez, E. Gallagher, J. Morrison, M. J. Austin, T. M. Scott, and N. Senechal. Mean Lagrangian flow behavior on an open coast rip-channeled beach: A new perspective. *Marine Geology*, 268(1):1–15, 2010. doi: 10.1016/j.margeo.2009.09.011.

R. Mannela. Integration of stochastic differential equations on a computer. *International Journal of Modern Physics*, C13(09):1177–1194, 2002. doi: 10.1142/S0129183102004042.

G. Masselink and A. Kroon. Morphology and morphodynamics of sandy beaches. *Coastal Zones and Estuaries. Encyclopedia of Life Support Systems*, pages 221–243, 2009.

K. McElwee, M. J. Donohue, C. A. Courtney, C. Morishige, and A. Rivera-Vicente. A strategy for detecting derelict fishing gear at sea. *Marine Pollution Bulletin*, 65 (1):7–15, 2012. ISSN 0025-326X. doi: 10.1016/j.marpolbul.2011.09.006.

C. C. Mei. *The Applied Dynamics of Ocean Surface Waves*, volume 1. World Scientific Singapore, 1992. doi: 10.1142/0752.

F. T. Moreira, D. Balthazar-Silva, L. Barbosa, and A. Turra. Revealing accumulation zones of plastic pellets in sandy beaches. *Environmental Pollution*, 218:313–321, 2016. ISSN 0269-7491. doi: 10.1016/j.envpol.2016.07.006.

M. Moulton, S. H. Suanda, J. C. Garwood, N. Kumar, M. R. Fewings, and J. M. Pringle. Exchange of plankton, pollutants, and particles across the nearshore region. *Annual Review of Marine Science*, 15(1):167–202, 2023. doi: 10.1146/annurev-marine-032122-115057.

A. B. Murray. *Contrasting the Goals, Strategies, and Predictions Associated with Simplified Numerical Models and Detailed Simulations*, chapter 3, pages 151–165. American Geophysical Union (AGU), 2003. ISBN 9781118668559. doi: 10.1029/135GM11.

W. Rattanapitikon and T. Shibayama. Simple model for undertow profile. *Coastal Engineering Journal*, 42(1):1–30, 2000. doi: 10.1142/S057856340000002X.

A. Reniers, E. Thornton, T. Stanton, and J. Roelvink. Vertical flow structure during sandy duck: observations and modeling. *Coastal Engineering*, 51(3):237–260, 2004. ISSN 0378-3839. doi: 10.1016/j.coastaleng.2004.02.001.

A. Reniers, J. Macmahan, E. Thornton, T. Stanton, M. Henriquez, J. Brown, J. Brown, and E. Gallagher. Surf zone surface retention on a rip-channeled beach. *Journal of Geophysical Research*, 114, 10 2009. doi: 10.1029/2008JC005153.

J. Schönhofer and A. Dudkowska. Rip currents in the southern Baltic Sea multi-bar nearshore zone. *Continental Shelf Research*, 212:104324, 2021. ISSN 0278-4343. doi: 10.1016/j.csr.2020.104324.

R. L. Soulsby. *Dynamics of Marine Sands*, pages 1–21. Thomas Telford, London, U. K, 1997. doi: 10.1680/doms.25844.fm.

G. G. Stokes. On the theory of oscillatory waves. *Transactions of the Cambridge Philosophical Society*, 8:441, 1847.

I. Svendsen. Mass flux and undertow in a surf zone. *Coastal Engineering*, 8(4): 347–365, 1984. ISSN 0378-3839. doi: 10.1016/0378-3839(84)90030-9.

I. A. Svendsen. *Introduction to Nearshore Hydrodynamics.* World Scientific, 2005. doi: 10.1142/5740.

D. J. P. Swift. *Nearshore Hydrodynamics and Sedimentation*, pages 563–568. Springer US, New York, NY, 1984. ISBN 978-0-387-30843-2. doi: 10.1007/0-387-30843-1_295.

The Open University. *Waves, tides and shallow-water processes. Butterworth-Heinemanns.* Butterworth-Heinemann, Oxford, 1999. doi: 10.1016/b978-0-08-036372-1.x5000-4.

E. B. Thornton and R. T. Guza. Transformation of wave height distribution. *Journal of Geophysical Research: Oceans*, 88(C10):5925–5938, 1983. doi: 10.1029/JC088iC10p05925.

L. Van Cauwenberghe, A. Vanreusel, J. Mees, and C. R. Janssen. Microplastic pollution in deep-sea sediments. *Environmental Pollution*, 182:495–499, 2013. ISSN 0269-7491. doi: https://doi.org/10.1016/j.envpol.2013.08.013.

W. G. Van Dorn. Breaking invariants in shoaling waves. *Journal of Geophysical Research: Oceans*, 83(C6):2981–2988, 1978. doi: 10.1029/JC083iC06p02981.

E. van Sebille, S. Aliani, K. L. Law, N. Maximenko, J. M. Alsina, A. Bagaev, M. Bergmann, B. Chapron, I. Chubarenko, A. Cózar, P. Delandmeter, M. Egger, B. Fox-Kemper, S. P. Garaba, L. Goddijn-Murphy, B. D. Hardesty, M. J. Hoffman, A. Isobe, C. E. Jongedijk, M. L. A. Kaandorp, L. Khatmullina, A. A. Koelmans, T. Kukulka, C. Laufkötter, L. Lebreton, D. Lobelle, C. Maes, V. Martinez-Vicente, M. A. M. Maqueda, M. Poulain-Zarcos, E. Rodríguez, P. G. Ryan, A. L. Shanks, W. J. Shim, G. Suaria, M. Thiel, T. S. van den Bremer, and D. Wichmann. The physical oceanography of the transport of floating marine debris. *Environmental Research Letters*, 15(2):023003, 2020. doi: 10.1088/1748-9326/ab6d7d.

L. C. Woodall, A. Sanchez-Vidal, M. Canals, G. L. Paterson, R. Coppock, V. Sleight, A. Calafat, A. D. Rogers, B. E. Narayanaswamy, and R. C. Thompson. The deep sea is a major sink for microplastic debris. *Royal Society Open Science*, 1(4): 140317, 2014. doi: 10.1098/rsos.140317.

J. Yu and D. Slinn. Effects of wave-current interaction on rip currents. *Journal of Geophysical Research*, 108, 2003. doi: 10.1029/2001JC001105.

H. Zhang. Transport of microplastics in coastal seas. *Estuarine, Coastal and Shelf Science*, 199:74–86, 2017. ISSN 0272-7714. doi: 10.1016/j.ecss.2017.09.032.
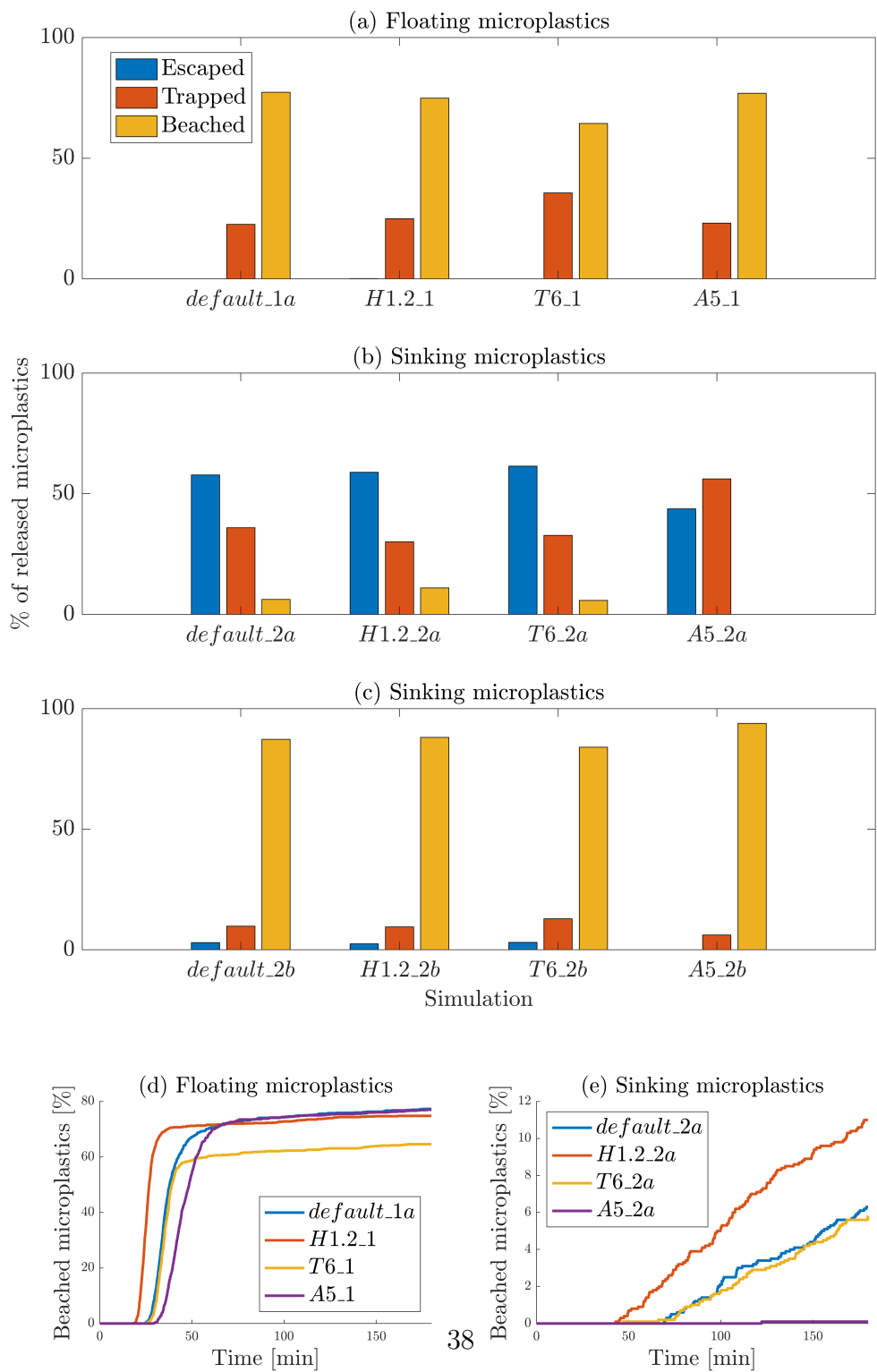
Figure C.16: (a)-(c) Fate of microplastics (escaped, trapped, beached) depending on input environmental conditions. Fate of (a) floating microplastics released offshore, (b) sinking microplastics released offshore, and (c) sinking microplastics released close to the shoreline is shown. (d)-(e) Percentage of released microplastics arriving at the shoreline as a function of time for different experiments. The plots show results for (a) floating microplastics released offshore and (b) sinking microplastics released offshore in Experiments $default\_1a$ and $default\_2a$ (blue line), $H1.2\_1$ and $H1.2\_2a$ (orange line), $T6\_1$ and $T6\_2a$ (yellow line), and $A5\_1$ and $A5\_2a$ (purple line). Note the different range of the vertical axis.

38